



ACADÉMIE  
DES SCIENCES  
INSTITUT DE FRANCE

# *Comptes Rendus*

---

## *Physique*

Adrien Lefauve


**Geophysical stratified turbulence and mixing in the laboratory**

Published online: 30 September 2024

**Part of Special Issue:** Geophysical and astrophysical fluid dynamics in the laboratory

**Guest editors:** Stephan Fauve (Laboratoire de Physique de l'ENS, CNRS, PSL Research University, Sorbonne Université, Université Paris Cité, Paris, France) and Michael Le Bars (CNRS, Aix Marseille Univ, Centrale Marseille, IRPHE, Marseille, France)

<https://doi.org/10.5802/crphys.196>

 This article is licensed under the  
CREATIVE COMMONS ATTRIBUTION 4.0 INTERNATIONAL LICENSE.  
<http://creativecommons.org/licenses/by/4.0/>



*The Comptes Rendus. Physique are a member of the  
Mersenne Center for open scientific publishing*  
[www.centre-mersenne.org](http://www.centre-mersenne.org) — e-ISSN : 1878-1535



Review article / *Article de synthèse*

Geophysical and astrophysical fluid dynamics in the laboratory /  
*Dynamique des fluides géophysiques et astrophysiques au  
laboratoire*

# Geophysical stratified turbulence and mixing in the laboratory

*Turbulence et mélange stratifiés géophysiques en  
laboratoire*

Adrien Lefauve<sup>a</sup>

<sup>a</sup> Department of Applied Mathematics and Theoretical Physics, University of  
Cambridge, United Kingdom  
E-mail: lefauve@damtp.cam.ac.uk

**Abstract.** Geophysical fluid flows that are stably-stratified in density, like most of the ocean, can be strongly turbulent at small scales as a result of shear instabilities. The resulting mixing controls the vertical transport of heat and tracers that are key to large-scale layering and circulation patterns, including those crucial to Earth's climate. However, the physics of sheared stratified turbulence remain poorly understood due to their extraordinary range of scales and spatio-temporal intermittency. This paper reviews a laboratory model, the stratified inclined duct (SID), which encapsulates these fundamental physics and complexity while permitting precise control and measurements, a sweet spot to stimulate fruitful research. We explain how this exchange flow down a modest slope sustains high levels of energy dissipation and mixing while remaining strongly-stratified, thereby accessing the relevant geophysical parameter regime. Emphasising the role of detailed measurements, we highlight key discoveries and unsolved questions around the transition to turbulence, intermittent dynamics and parameterisations of mixing. Dimensional design guidelines show how the optical measurements of the full three-dimensional flow field could be perfected to extrapolate laboratory results to the tantalisingly close regime of the most intense geophysical stratified turbulence.

**Résumé.** Les écoulements géophysiques de fluides qui sont stablement stratifiés en densité, comme la plupart de l'océan, peuvent être fortement turbulents à petite échelle en raison d'instabilités de cisaillement. Le mélange qui en résulte contrôle le transport vertical de la chaleur et des traceurs qui sont essentiels pour la stratification et la circulation à grande échelle, et donc pour notre climat. Cependant, la physique de la turbulence stratifiée cisailée reste mal comprise en raison de sa gamme d'échelles extraordinaire et de son intermittence spatio-temporelle. Cet article passe en revue un modèle de laboratoire, le conduit incliné stratifié (SID), qui capture les fondamentaux de cette physique et sa complexité tout en permettant un contrôle et des mesures précis, une combinaison optimale pour stimuler des recherches fructueuses. Nous expliquons comment cet écoulement d'échange le long d'une pente modeste maintient une dissipation turbulente et un mélange élevés tout en restant fortement stratifié, accédant ainsi au régime géophysique pertinent. En mettant l'accent sur le rôle de mesures détaillées, nous soulignons les découvertes clés et les nombreuses questions non résolues autour de la transition vers la turbulence, des dynamiques intermittentes et des paramétrisations du mélange. Le dimensionnement expérimental montre comment perfectionner les mesures optiques tridimensionnel de l'écoulement pour extrapoler ces résultats au régime le plus intense de la turbulence stratifiée géophysique, qui est enfin à portée de main.

**Keywords.** turbulence, mixing, geophysical, shear, instability, intermittency, ocean, parameterisation.

**Mots-clés.** turbulence, mélange, géophysique, cisaillement, instabilité, intermittence, océan, paramétrage.

**Funding.** The author is supported by a NERC Independent Research Fellowship NE/W008971/1. The experimental facilities were funded by an EPSRC Programme Grant EP/K034529/1 (2013-2018) and an ERC Horizon 2020 Grant No 742480 (2018-2023).

*Manuscript received 3 May 2024, revised 19 July 2024, accepted 5 August 2024.*

## 1. Introduction

Turbulence in density-stratified environments plays a central role in geophysical and astrophysical fluid dynamics (GAFD) because it enhances the transport of heat, mass and momentum several orders of magnitude above molecular values. This turbulent transport shapes the bulk properties, spatial structure and temporal evolution of stars, planetary cores, atmospheres, oceans and freshwater bodies, which are often physically and/or chemically heterogeneous, and thus layered in density.

This paper focuses on stably-stratified turbulence generated by a large-scale free shear, a canonical GAFD problem alongside, for example, boundary layer turbulence (affected by the presence of a solid boundary) or thermal convection (driven by an unstable stratification). Stably-stratified shear-driven turbulence (hereafter simply “stratified turbulence”) is responsible for most of the mixing in Earth’s ocean interiors and coastal waters, as it mediates the transfer of energy between large-scale currents or internal waves and small-scale mixing by molecular diffusion [1]. The irreversible homogenisation of temperature, salinity and passive tracers, and the efficiency of this process, are crucial to our environment and climate. This is because mixing not only controls regional-scale water composition but also the global circulation of our oceans, the rate at which they draw and sequester atmospheric heat and carbon, upwell nutrients, and thereby shape the biogeochemical cycles on which life depends [2].

Over a century of research in the physics of turbulent mixing revealed that this nonlinear transfer of energy is highly sensitive to the details of the flow – not only to the overall geometry and bulk dimensionless parameters, but also to details in the boundary conditions, the source of energy feeding the turbulence, the instabilities causing the transition to turbulence, the flow history, etc. As a result, it is frustratingly difficult to say anything generic about stratified turbulence and mixing, a theoretical hurdle which limits practical parameterisations of mixing in general circulation models [3, 4]. An improved physical understanding of small-scale stratified turbulent mixing is thus necessary to improve the scientific credibility and interpretation of models. It is also important to reduce the uncertainty and increase the public confidence in climate predictions and mitigation measures [5].

A few generic statements can nevertheless be made about stratified turbulence in order to contrast it to classical turbulence. The restoring buoyancy force in the momentum equation and the potential energy cost associated with vertical motions have at least three far-reaching consequences. First, stratified turbulence is distinctively intermittent, and connected with internal gravity waves and their associated temporal scales [6]. Second, it is more anisotropic and prone to the formation of vertical well-mixed layers separated by sharp interfaces – a pattern that produces vertical velocity and density gradients higher than horizontal ones [7]. Third, it has a wider and richer spectrum of dynamically important length scales [8]. The Ozmidov scale, below which stratification ceases to be felt by eddies, is located between the integral (production) scale of the largest eddies and the dissipation (or Kolmogorov) scale. The Batchelor scale, signalling where molecular diffusion occurs, is typically located below the dissipation scale. These three generic

properties make the direct numerical simulations of sustained, stratified turbulence in the parameter regime relevant to GAFD very challenging [9–11]. Physicists, therefore, need relatively simple laboratory experiments in which stratified turbulence can be generated, carefully controlled and accurately measured. Simple, canonical laboratory models such as pipe flow [12], Rayleigh–Bénard flow [13] and Taylor–Couette flow [14] have long been vital playgrounds to develop and test new theories of turbulence, and as such they are the “drosophila” of turbulence research [15]. A “drosophila” flow should capture the essence of the “real-world” problem of ultimate interest while retaining enough realism and complexity to be a stimulating and fruitful long-term research challenge attracting a diverse group of researchers. This experimental tradition in fluid dynamics draws its power from dimensional analysis, which enables us to extrapolate the turbulent properties from the laboratory scale to the geophysical scale of interest. However, devising such extrapolation models necessitates a deep understanding of the complex physics at play in a realistic flow, of the peculiarities of its boundary conditions and scaling laws, and of the practical setup and measurements techniques – an understanding that can only be gained from a sustained community effort requiring a critical mass.

This paper surveys a relatively recent “drosophila” for stratified turbulence research, the stratified inclined duct (SID) experiment, introduced 10 years ago by Meyer and Linden [16]. This paper has three objectives. First, to explain why SID represents an effective and versatile laboratory model to improve the GAFD community understanding of stratified turbulence. Second, to convey the substantial physical understanding gained in the last 10 years, with an emphasis on the measurements that contributed to it. Third, to exhibit the wealth of open questions raised in the process, and to guide researchers in the design of further experiments to answer them.

With these objectives in mind, we introduce SID in Sec. 2, with its historical roots and dimensionless framework. In Sec. 3, we focus on the three types of measurements that shaped our “first-order” physical understanding, before touching on more advanced “second-order” findings and open questions in Sec. 4. In Sec. 5, we leverage this understanding to explain how SID should be scaled up for stronger geophysical turbulence, translating dimensionless scaling laws to physical units and practical design guidelines. Finally, we conclude in Sec. 6.

## 2. The Stratified Inclined Duct (SID)

### 2.1. *History: from a transient to a sustained flow*

An early attempt to study the transition to turbulence in a stably-stratified flow dates back to Reynolds’s seminal paper in 1883 [17] on turbulence in pipe flow. In the lesser known § 12, he contrasted the instability in unidirectional pipe flow to that observed in a stratified counterflow generated between two immiscible liquid layers upon tilting the pipe (see Figure 1 (a)). In the late 1960s, Thorpe [18] studied the Kelvin–Helmholtz instability of a shear layer and its breakdown to turbulence by tilting a rectangular tank initially filled with salt solutions at different densities (Figure 1 (b)). Both of these experiments are by nature transient and short-lived because of the limited longitudinal extent of the apparatus.

The Stratified Inclined Duct (SID) proposed by Meyer and Linden in 2014 [16] overcomes this limitation by adding large reservoirs on either side of a long rectangular duct to sustain a long-lived exchange flow (Figure 1 (c)). (Note that a similar setup was described by Macagno and Rouse in 1961 [19] but their paper was not widely disseminated.) Importantly, the apparatus can be tilted at a small angle  $\theta$  to force the denser layer to accelerate as it flows downslope and vice versa. Whether the apparatus is tilted or not, SID creates a virtually pure (“baroclinic”) exchange flow with no net (“barotropic”) component; in other words, the reservoirs exchange buoyancy but keep a constant volume. As we shall see, the originality of SID is that the simple, natural



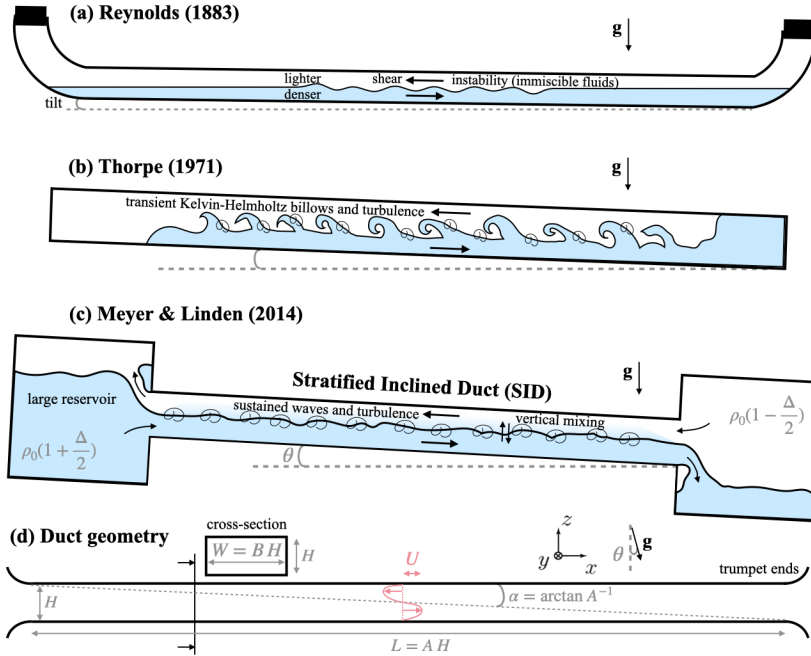


**Figure 1.** Early experiments on stratified turbulence compared to the more recent Stratified Inclined Duct (SID) discussed in this paper. The reservoirs on either side of a long rectangular duct sustain an exchange flow for long times, forced by a tilt  $\theta$ .

forcing of gravity through  $\theta$  sustains for very long times statistically stationary and vigorous interfacial stratified turbulence that long seemed out of reach of either laboratory or numerical experiments [7].

Following the classification of Turner [20, § 4.3.1], SID turbulence is an example of “internal mixing process” [20, § 4.1.4., § 10] because it is fed by the mean shear, which is itself a consequence of the stratification. This leads to a self-sustaining local equilibrium between turbulence, shear, stratification and mixing, typical of geophysical flows. Other laboratory experiments studied turbulent entrainment by relying either on pumps to generate the shear, resulting in a different kind of equilibrium [21–23], or by relying on “external mixing processes” using oscillating grids, rakes or a surface stress (see [20, § 9.1], [4, § 7]).

## 2.2. Dimensionless numbers

The first parameter driving SID flow is the reduced gravity  $g' = g \Delta$  where  $\Delta$  is the dimensionless density difference. By convention the left reservoir has density  $\rho_0(1 + \Delta/2)$  and the right reservoir has density  $\rho_0(1 - \Delta/2)$  (where  $0 < \Delta \ll 1$ ), noting that  $\Delta/2$  is sometimes called the Atwood number. The second obvious parameter is the tilt angle  $\theta$ , usually kept below  $\approx 0.2$  rad (corresponding to  $\approx 11^\circ$ ) to remain in the “stably-stratified” realm (in which we assume  $\cos \theta \approx 1$  and  $\sin \theta \approx \tan \theta \approx \theta$ ). The duct geometry (Figure 1 (d)) also plays an important role. In order of decreasing dynamical importance, we define the duct height  $H$ , length  $L = AH$  and width  $W = BH$  and impose that the streamwise aspect ratio be very large  $A > 10$ , while the spanwise aspect ratio

tends to be  $B = O(1)$  (say between 1/4 and 4). At times, it will prove useful to interpret the aspect ratio  $A$  as a slope  $\alpha = \arctan(A^{-1}) \approx A^{-1} \ll 1$  radian (see dashed line in Figure 1 (d)). These parameters are summarised in Table 1.

In the last 10 years, three generations of apparatus have been used in the G. K. Batchelor Laboratory in Cambridge, as well as multiple duct geometries, with heights  $H$  between 45 mm and 100 mm,  $A = 15, 30, 40$  and  $B = 1/4, 1$  and 2. (See [16] for the first generation, see [24] for the second generation, see [25] for a summary of the data in both, and see [26] for the third generation.) The ends of the duct can either be sharp or trumpet-shaped without greatly affecting the flow in the duct away from the ends.

Importantly, SID does not have an intrinsic velocity scale. The flow is driven by the reduced gravity  $g\Delta$ . The observed velocity scale, which we can take as the peak exchange velocity  $U$  (figure 1d) must be set by a dominant balance between the terms in the along-duct ( $x$ ) momentum equation [25]; these are the inertia  $\sim U^2/L$ , the hydrostatic pressure gradient driving the exchange  $\sim g\Delta H/L = g\Delta\alpha$  (an acceleration down the slope  $\alpha$ ), the additional downslope acceleration  $g\Delta\theta$ , and the viscosity  $\nu U/H^2$ , where  $\nu$  is the kinematic viscosity. As we are interested in turbulent flows, the dominant balance must include the inertial rather than the viscous term, but it is not a priori clear whether it should be balanced by the hydrostatic term, giving  $U \sim (g\Delta H)^{1/2}$ , or by the gravitational term, giving  $U \sim (g\Delta L\theta)^{1/2}$ . As we shall see, experiments revealed early on that it was the former, i.e. an inertial-hydrostatic scaling, with the tilt  $\theta$  and viscosity  $\nu$  playing a more minor role in regulating the exchange. In SID, the along-duct velocity scale is  $U = (g\Delta H)^{1/2}$ , corresponding to a “free fall” from the duct height  $H$  rather than from the duct elevation  $L\theta$ .

**Table 1.** Summary of the parameters and scales used to make the analysis dimensionless, such that the vertical coordinate  $\tilde{z}$ , the streamwise velocity  $\tilde{u}$  and the density  $\tilde{\rho}$  are all bounded by  $\pm 1$ .

---

### Input parameters

#### Dimensional

$g' = g\Delta$	Reduced gravity ( $\Delta$ is the dimensionless density difference)
$H, L, W$	Duct height, length and width
$\nu, \kappa$	Kinematic viscosity and scalar diffusivity

#### Dimensionless

$\theta$	Duct tilt set by the experimenter
$Re = (g\Delta H^3)^{1/2} / (2\nu)$	Reynolds number
$Pr = \nu/\kappa$	Prandtl number
$A \approx \alpha^{-1}$	Streamwise aspect ratio ( $\alpha$ is the duct geometric slope)
$B$	Spanwise aspect ratio

### Scales for normalisation

$H/2$	Length scale: thickness of each layer and of the shear layer
$U = (g\Delta H)^{1/2}$	Velocity scale: maximum velocity expected in each layer
$H/(2U) = [H/(g\Delta)]^{1/2} / 2$	Time scale: inverse of the bulk shear
$g'/2 = g\Delta/2$	Buoyancy scale : half of the maximum difference (leading to a bulk buoyancy time scale of $[H/(g\Delta)]^{1/2}$ and a bulk Richardson number $Ri = 1/4$ )

---

We can now add to our existing set of dimensionless parameters ( $\theta$ ,  $A$  or  $\alpha$ , and  $B$ ), the Reynolds number  $Re$  based on  $U$  and the typical layer thickness  $H/2$  as well as the Prandtl number  $Pr$ :

$$Re = \frac{UH}{2\nu} = \frac{(g\Delta H^3)^{1/2}}{2\nu}, \quad Pr = \frac{\nu}{\kappa}. \quad (1)$$

For practical reasons, SID has traditionally been run with salt, having very low diffusivity  $\kappa$ , in which case  $Pr = 700$ , but it has also been run with temperature stratification, in which case  $Pr = 7$  (note that we take a reference value of  $\nu = 1.05 \times 10^{-6} \text{ m}^2 \text{ s}^{-1}$  for water at a room temperature of  $20^\circ\text{C}$ ). Scaling all the flow variables accordingly (see Table 1), we create dimensionless “tilde” variables for the spatial coordinates  $\mathbf{x} = (x, y, z) = (H/2)\tilde{\mathbf{x}}$ , velocity  $\mathbf{u} = (u, v, w) = U\tilde{\mathbf{u}}$ , time  $t = U/(H/2)\tilde{t}$  and density variations around the neutral density  $\rho = \rho_0[1 + (\Delta/2)\tilde{\rho}]$  (i.e.,  $-\tilde{\rho}$  is a buoyancy). The dimensionless equations of motion are:

$$\tilde{\nabla} \cdot \tilde{\mathbf{u}} = 0, \quad \frac{\partial \tilde{\mathbf{u}}}{\partial \tilde{t}} + \tilde{\mathbf{u}} \cdot \tilde{\nabla} \mathbf{u} = -\tilde{\nabla} \tilde{p} + \frac{1}{Re} \nabla^2 \tilde{\mathbf{u}} + Ri \tilde{\rho} (\theta \mathbf{e}_x - \mathbf{e}_z), \quad \frac{\partial \tilde{\rho}}{\partial \tilde{t}} + \tilde{\mathbf{u}} \cdot \tilde{\nabla} \tilde{\rho} = \frac{1}{Re Pr} \tilde{\nabla}^2 \tilde{\rho}, \quad (2)$$

expressing incompressibility, conservation of momentum (Navier–Stokes) and the coupled buoyancy transport, under the Boussinesq approximation that  $0 < \Delta \ll 1$  (recall that in the gravity forcing, we assume  $\cos\theta \approx 1$  and  $\sin\theta \approx \theta$ , in radians). The buoyancy is coupled to the momentum through the bulk Richardson number  $Ri = g(\Delta/2)(H/2)/U^2$ . In SID, it is essentially fixed at  $Ri = 1/4$  by the scaling  $U = (g\Delta H)^{1/2}$ . Another interpretation is that the bulk buoyancy frequency  $U/H = (g\Delta H^{-1})^{1/2}$  is half the mean shear used to make time dimensionless.

Importantly, the Reynolds number in (1) is a prognostic parameter set by the experimenter, assuming  $U = (g\Delta H)^{1/2}$ , rather than a diagnostic parameter using measured values. This choice has the advantage of simplicity, but when it was desirable to compare the evolution of detailed flow properties with  $Re$  across a range of experiments, and when detailed velocity measurements were available, we have also used a carefully defined, diagnostic “shear layer” Reynolds number [27]. Drawing a parallel with vertical convection [28], it is possible to approximate SID as a closed duct having Dirichlet boundary conditions  $\tilde{\rho} = \pm 1$  on the left and right boundaries  $\tilde{x} = \mp A$  sustaining the exchange. This problem is well defined by the (prognostic) Rayleigh number  $Ra = g\Delta H^3/(\nu\kappa)$ , and our Reynolds number (1) is equivalent to the scaling  $Re = Ra^{1/2} Pr^{-1/2}$ .

Compared to a lock exchange gravity current down a slope [29, 30], SID differs in that its large reservoirs allow it to access the stationary stratified shear flow established after the initial gravity currents have exited the duct. The gravity current dynamics last a time  $L/U = (L/H)(H/U)$  i.e. only  $A$  shear time scales and are sensitive to the behaviour of the head of the current and to initial conditions. These initial transients are discarded in SID experiments to focus on the long-time dynamics of the ensuing shear flow. These dynamics are insensitive to the initial conditions and to the plume dynamics in the reservoirs, as we will see next.

### 3. Experimental methods and first-order findings

#### 3.1. Shadowgraphs: flow regimes and interfacial mixing

The simplicity of SID allowed Meyer and Linden [16] to explore the parameter space ( $Re, \theta$ ) (in their original paper  $(\Delta, \theta)$ ), where they discovered various flow regimes. To visualise the flow, they used the simple shadowgraph technique (see Figure 2 (a)), in which the experimenter illuminates a central section of the duct with nearly parallel light, and records with a camera the pattern of shadows resulting from density-related refractive index variations inside the duct. Shadowgraphs are well-suited for the detection of sharp density contrasts within the flow, caused by interfacial waves, turbulence and mixing. (Shadowgraphs from many of their experiments, and more recent ones, are shared in the repository [33].)

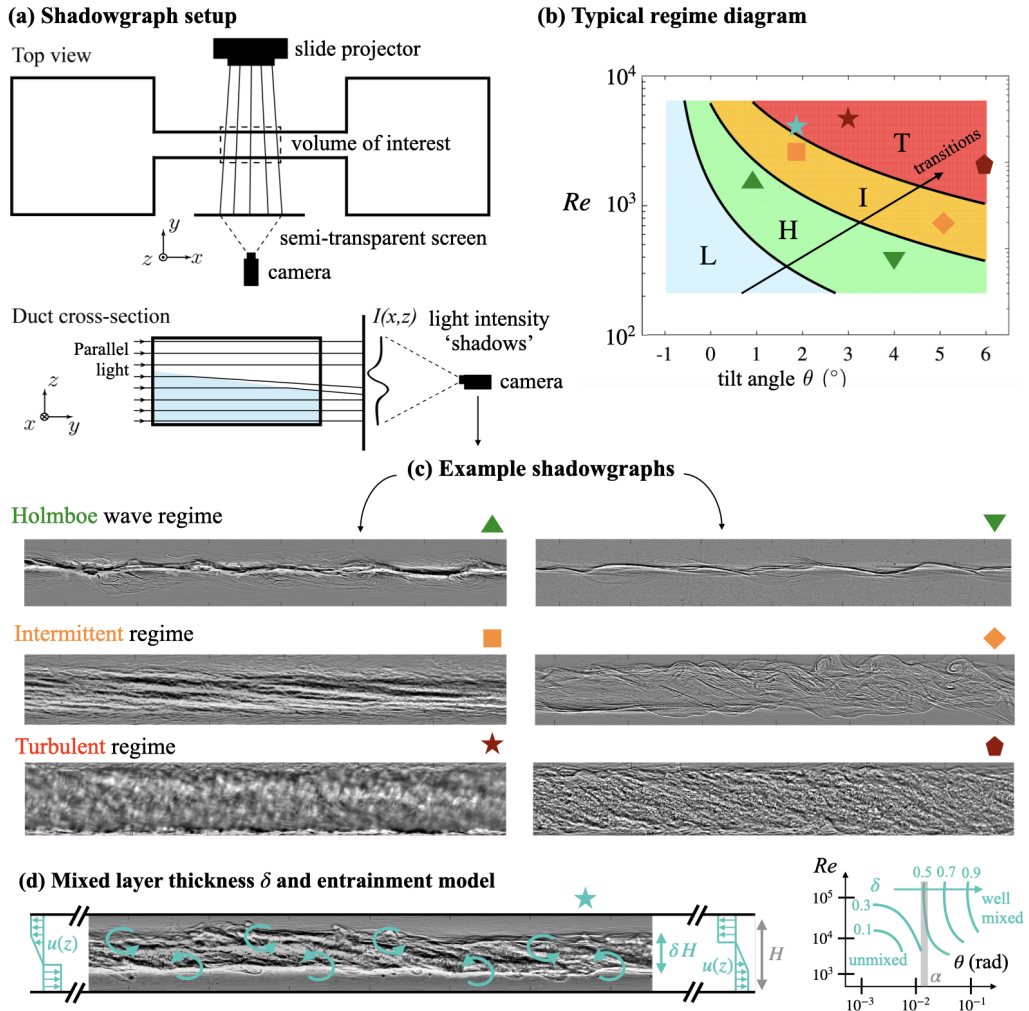


**Figure 2.** (a) Shadowgraphy exploit the refraction of initially parallel light to visualise density contrasts within the flow [31]. (b) This technique was instrumental in mapping the multiple flow regimes in parameter space: Laminar, Holmboe waves, Intermittently turbulent, Turbulent (originals in [25]). (c) Visualisations in different regions of parameter space (see matching symbols in (b)) highlight the diversity of SID dynamics idealised regime diagram (data in [32]). (d) Shadowgraph also helped model the thickness of the interfacial mixed layer (see Sec. 3.1 and [25]).

The regimes they identified are mapped in a typical  $(Re, \theta)$  “regime diagram” in Figure 2(b) and are illustrated by representative snapshots in Figure 2(c). These regimes, are, by order of increasing  $Re$  and  $\theta$ : laminar two-layer flow with a sharp, stable interface (snapshot not shown); wavy flow with an unstable but still sharp interface featuring travelling “Holmboe” waves (“H” regime); wave breaking and intermittent bursts of interfacial turbulence with complex spatio-temporal patterns (“I”); fully-developed and sustained interfacial turbulence with a thick, partially mixed layer (“T”). The discovery and qualitative description of these regimes were influential as they showed that SID harbours a wealth of flow behaviours – internal waves,

intermittency and anisotropic layering – that are the hallmark of stratified turbulence. Moreover, comparing the snapshots in the left and right columns of Figure 2 (c) reveals that even within the broad H, I and T “territories”, flow in different subregions can be very different, thus begging for a finer classification of regimes.

To this end, an automated, data-driven classification was performed in [26] using a newer, curated dataset of 113 long shadowgraph movies covering the parameter space (shared in the repository [32]). The method was applied frame by frame and combined edge detection to extract fine-scale density interfaces, physically-interpretability dimensionality reduction based on the morphology of these interfaces, and unsupervised clustering to identify dense regions in the reduced space. Subtly different turbulent states were revealed and interpreted, with gradual shifts in their distribution across parameter space, as well as different temporal routes between them in the intermittent regime. These results further highlighted the richness of the dynamics present in SID and the potential of machine learning techniques to assist the human eye in extracting physical insights from large laboratory datasets.

Shadowgraphs were also used in [25] to systematically estimate the thickness of the partially mixed layer, which we define as a dimensionless ratio  $\delta \in [0, 1]$  of the duct height (Figure 2 (d)). A simple entrainment model (see cyan profiles) was developed to explain empirical scaling laws for the scaling of  $\delta(Re, \theta)$  in the dataset [33], as well as earlier data at very large  $Re > 10^5$  in an earlier SID-like experiment [34]. The layer  $\delta$  was assumed to be linearly stratified, and each counterflowing layer was assumed to enter the duct unmixed with a “plug”, irrotational velocity and to leave the duct by carrying the mixed fluid out with a linear velocity. The balance between the turbulent entrainment of unmixed fluid, its mixing with an efficiency  $\Gamma \in [0, 1]$ , and its out-flow yields a steady-state thickness

$$\delta \approx [(3/2)\theta A \Gamma]^{1/3} \approx 0.5(\theta/\alpha)^{1/3} \text{ for } Re > 10^5, \quad (3)$$

assuming  $\Gamma(Re) \rightarrow 0.1$  for  $Re > 10^5$ , a 10 % efficiency consistent with data from lock-release gravity currents [35]. To first order, the mixed layer thickness therefore depends only on the ratio of the duct’s tilt  $\theta$  to its geometrical slope  $\alpha$ , as long as  $Re$  is large enough (Figure 1 (d)). As a rule of thumb, the mixed layer thus fills half the duct height ( $\delta \approx 0.5$ ) when  $\theta \approx \alpha$ .

### 3.2. Mass flux: hydraulic control and transition

The observed distribution of flow regime “territories” in  $(Re, \theta)$  space raised the question: what controls the transitions, shown by black curves in Figure 2 (b)? An important clue to answer this question was the behaviour of the dimensionless mass flux  $Q_m$ , which quantifies the average amount of mass (more specifically, buoyancy) exchanged along the duct:

$$Q_m = \langle \tilde{\rho} \tilde{u} \rangle_{x,y,z,t}, \quad (4)$$

where  $\langle \cdot \rangle_{x,y,z,t}$  denotes averaging over the duct volume and over a sufficiently long time. We bear in mind that this baroclinic exchange has a zero net barotropic exchange  $\langle \tilde{u} \rangle_{x,y,z,t} = 0$ . This mass flux is a key diagnostic parameter in SID, akin to the Nusselt number in convection.

Measurements of  $Q_m$  were performed as sketched in Figure 3 (a). Initially, the reservoirs were filled with salt solutions having an initial density difference  $\Delta\rho^i$ . The duct was typically filled with fluid at intermediate density, but initial conditions were soon forgotten after the initial transients and thus unimportant for the long-time evolution of the flow. The gates on either side of the duct were then opened, the exchange flow of interest allowed to run for a time  $\tau$ , before the gates were closed and the reservoirs were mixed. The difference between the initial and final density in both reservoirs  $\Delta\rho^f$  (which should be equal) was then measured with a high-precision density meter to compute the mass exchanged  $\Delta m$  and the dimensionless  $Q_m$  (details in Figure 3 (a) and



always remain shallower than  $\alpha$  as it is bounded by the duct walls. In this “lazy flow”, the convective acceleration of each layer along the duct results in a maximum layer-averaged velocity and interfacial offset at the outlets, where the geometry expands rapidly. This results in a locally supercritical flow, against which the waves cannot travel. (Technically, supercritical flow is flagged by a “composite” (two-layer) Froude number  $> 1$  [37, 38], akin to the sound waves in a supersonic flow at Mach number  $> 1$ .) The flow is said to be in a state of hydraulic control because the supercritical outlet regions control the duct by isolating it from external information or disturbances (waves) coming from the reservoirs. Hydraulic control leads to a “maximal exchange” Froude number condition which translates to  $Q_m = 0.5$  in an inviscid laminar flow, but is reduced slightly by viscous friction at intermediate  $Re$  [39].

As  $\theta$  is increased above 0, hydrostatic balance (see orange lines in Figure 3(c)) tends to make the density interface slope upwards, partially countering the downward frictional slope, thereby forcing an increase in  $Q_m$  towards the hydraulic limit of 0.5. When  $\theta \approx \alpha$ , the upward forcing slope  $\theta$  dominates over the maximum possible downward friction slope  $\alpha$  [25]. This “forced flow” is then confronted to an inadmissible mid-duct ( $x = 0$ ) upward slope (which would decelerate each layer along the duct), giving rise to an internal hydraulic jump, akin to a shock wave in supersonic flow. Recent direct numerical simulations (DNS) of the flow along the duct [40] and their analysis in the framework of two-layer hydraulics [41] revealed that this forced flow is then mildly supercritical all along the duct. This leads to the unstable growth of stationary, long (hydrostatic) waves, followed by travelling, short (non-hydrostatic) waves that break, overturn and dissipate just enough energy to keep a zero mean interfacial slope.

As  $\theta$  is increased well above  $\alpha$  (Figure 3(d), turbulence intensifies in order for the viscous dissipation  $\propto Re^{-1}$  to keep up with and “regularise” the “inadmissible” upward tilt  $\theta$ . This balance leads to turbulence levels  $\propto Re \theta$  consistent with the regime transitions. The mean interface is thus always approximately parallel to the duct walls, i.e. the mean isopycnals (in blue) are always tilted by  $\theta$  relative to gravity (orange lines). This robust relative tilt sustains the baroclinic generation of spanwise vorticity, primarily shear  $\partial\tilde{u}/\partial\tilde{z}$ , which in turn sustains the turbulence and the mixed layer. DNS revealed that turbulence creates a zone of low pressure in the central half of the duct length (see yellow shade) [40]. This zone creates, for each layer, a large-scale adverse pressure gradient over the second half of their transit along the duct (see yellow arrows). This gradient balances the acceleration of the flow along the slope  $\theta$  with a matching deceleration, which prevents the “free fall” scaling from height  $L\theta$  (which would give  $U = (g\Delta L\theta)^{1/2} \Leftrightarrow Q_m = 0.5(\theta/\alpha)^{1/2}$ ) and enforces the maximal exchange condition  $Q_m \leq 0.5$  when  $\theta > \alpha$ . Increasingly intense turbulence for  $\theta \gg \alpha$  then decreases  $Q_m$  below 0.5, because turbulence transports salt from the right-flowing, dense bottom layer upwards into the left-flowing, light upper layer. Some of this vertical buoyancy flux translates to irreversible mixing by small-scale diffusion; thus some of the fluid ends up being advected back to the reservoir where it originates, decreasing the net longitudinal buoyancy flux  $Q_m$ . In fact, assuming self-similar, linear profiles for  $\tilde{u}, \tilde{\rho}$  in the mixed layer yields a  $Q_m$  decreasing linearly with  $\delta$ . This completes the “hydraulics” interpretation of regime transitions and mass flux data.

The resulting turbulent equilibrium across the shear layer (Figure 3(e)), in pink) can be characterised by a gradient Richardson number profile  $Ri_g(\tilde{z}) = N^2/S^2$  along the duct  $z$ -direction (Figure 3(g), in purple), the ratio of the squared buoyancy frequency  $N^2 = -(g'/H)\partial\langle\tilde{\rho}\rangle_{x,y,t}/\partial\tilde{z}$  (stabilising the flow) to the squared shear  $S^2 = (4g'/H)(\partial\langle\tilde{u}\rangle_{x,y,t}/\partial\tilde{z})^2$  (destabilising the flow). The linearly stratified mixed layer must have a mean  $-\partial\tilde{\rho}/\partial\tilde{z} \approx 1/\delta$ , while velocity measurements (detailed in the next section) show that the turbulent shear layer has a typical dimensionless thickness  $\approx \sqrt{2}$  and peak-to-peak velocity jump  $\approx \sqrt{5}$ , resulting in a mean  $(\partial\tilde{u}/\partial\tilde{z})^2 \approx 5/2$ . This

suggests an approximately uniform “equilibrium” Richardson number:

$$Ri_g(\bar{z}) = \frac{N^2}{S^2} \approx Ri_e = \frac{1}{4} \frac{(-\partial\tilde{p}/\partial\bar{z})}{(\partial\tilde{u}/\partial\bar{z})^2} \approx \frac{1}{4} \frac{1/\delta}{5/2} \approx \frac{1}{10\delta}. \quad (5)$$

We thus expect  $Ri_e \approx 1/4 = 0.25$  when  $\delta \approx 0.4$  (i.e. when  $\theta \approx \alpha/2$  according to (3)), noting that sustaining turbulence with such weak forcing requires  $Re > 10^4$ . However, we expect a lower  $Ri_e \approx 1/7 \approx 0.15$  when the mixed layer is thicker  $\delta \approx 0.7$  (i.e. when  $\theta \approx 3\alpha$ ). Sustaining turbulence with this strong forcing is possible at  $Re = O(10^3)$ , as shown next.

### 3.3. Volumetric velocimetry and density: energy budgets and dissipation

The last piece of the puzzle to complete our “first-order” understanding of the physics of SID came from analysing the kinetic and potential energy pathways of the flow. This analysis was made possible by a major technological advance, sketched in Figure 4 (a) and detailed in [42], which provided the time-resolved velocity and density fields simultaneously in three dimensions, at a high enough spatial resolution for the dynamically active scales to be captured.

These measurements are entirely optical and non-intrusive, relying on a dual-cavity Nd:YAG pulsed laser to illuminate a thin sheet of the flow in a central section of the duct. Microscopic, neutrally-buoyant reflective particles are seeded in the flow and imaged to determine the two-dimensional velocity field through Particle Image Velocimetry, or PIV (see “Raw PIV-B image”). Two images taken a short time interval apart are divided into small, partially overlapping, interrogation windows and compared window by window. The shift in the pattern of particles between successive frames yields a local velocity vector in each window. In order for particle images to remain sharp, the refractive indices are carefully matched by achieving the density difference with a pure sodium nitrate ( $\text{NaNO}_3$ ) solution in the dense reservoir and a pure sodium chloride ( $\text{NaCl}$ ) solution in the light reservoir [31]. (Note that matching refractive indices is not possible if the experiment is run with temperature stratification only.) To obtain the  $y$ -component of velocity (across the laser sheet), two cameras (PIV-A and PIV-B) are positioned at a angle to the plane of interest. Any motion along  $y$  appears to each camera as an apparent left or right motion, and  $v$  is calculated with suitable coordinate transformations. The result is a three-component, two-dimensional velocity field whose resolution depends on the size of the interrogation windows. Using video cameras with a resolution of 8 Mpixels and speed of 200 frames per second (to match the laser frequency),  $x - z$  planes containing  $400 \times 100$  three-dimensional vectors were output at a frequency of 100 Hz [42].

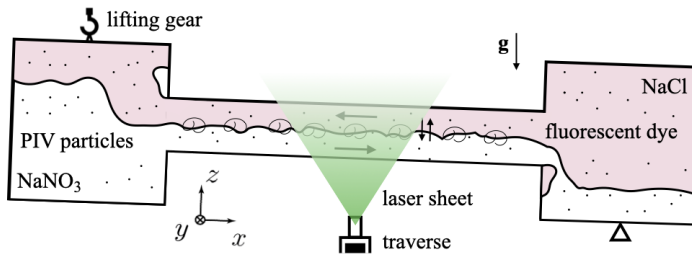
The density field is measured simultaneously in the same plane with Laser Induced Fluorescence (LIF), which relies on mixing the rhodamine 6G dye in one of the reservoirs (here on the right). The dye tagging the upper layer (see “Raw LIF” image) absorbs the 532 nm laser light and emits it back with a minor redshift, allowing optical filters to separate the dye and the particle signals. The fluid density is then calculated using an appropriate calibration and assuming that the passive dye concentration faithfully tags the active salinity field, since both have a very high  $Pr = O(10^3)$ . (This assumption would be questionable if the active scalar were temperature.)

The technological leap to obtain three-dimensional data was to continuously scan this laser sheet back and forth along  $y$  and combine PIV and LIF planes captured in quick succession into volumes. This scanning approach is advantageous in SID due to the requirement of measuring velocity and density simultaneously at high-resolution, which is impractical with other volumetric approaches [42]. A smooth, continuous scanning motion is necessary considering the speed and the inertia of the traverse-mounted carriage carrying the light sheet optics, and the sensitivity of these measurements to vibrations. But how can a fast and continuous scanning yield two overlapping laser sheets required to perform PIV? This challenge was overcome by introducing

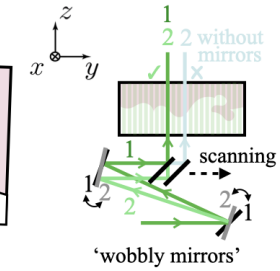


**(a) Setup for scanning, simultaneous PIV and LIF**

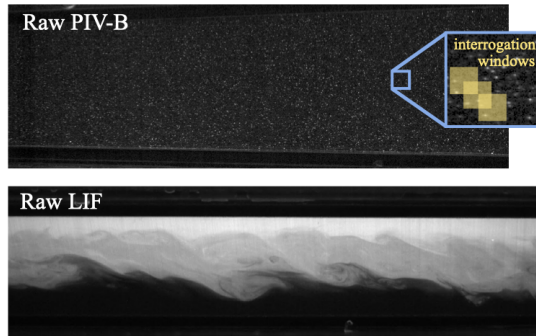
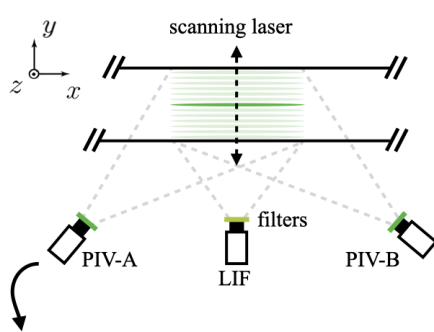
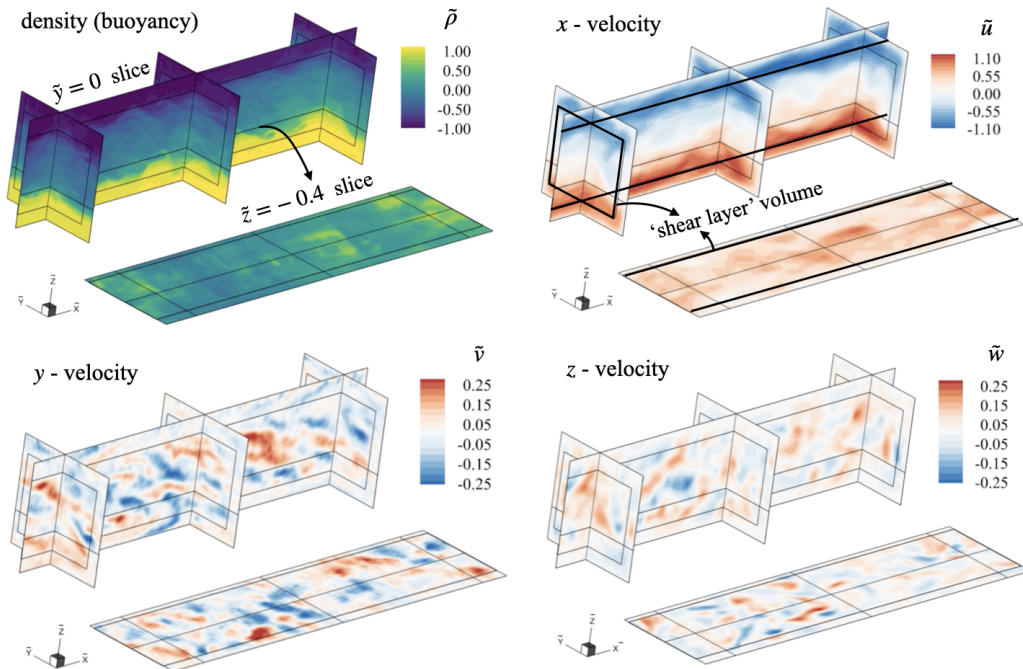
Side view



Cross-section



Top view

**(b) Processed volumetric data**

**Figure 4.** (a) Scanning technique combining simultaneous planar Particle Image Velocimetry (PIV) and Laser Induced Fluorescence (LIF) to measure the time-resolved, volumetric velocity and density fields. (b) Here we show a snapshot at  $Re = 1256$ ,  $\theta = 6^\circ \approx 3\alpha$  (datasets available at [43]). These data provide full access to the detailed flow energetics sketched in Figure 5, which were decisive to complete the first-order physical understanding of SID in Sec. 3.3.

a pair of rapidly oscillating mirrors mounted on galvanometers (“wobbly mirrors” in the cross-section view of Figure 4 (a)) that correct the position of the laser sheet to recover overlapping pairs of images [42]. The DigiFlow software [44] handled the hardware control, synchronisation of the laser pulses, traverse, wobbly mirrors, cameras, as well as the processing of PIV and LIF data.

The processed volumetric data in world coordinates are illustrated in Figure 4 (b) by a single “snaphsot” of  $(\tilde{\rho}, \tilde{u}, \tilde{v}, \tilde{w})(\tilde{x}, \tilde{y}, \tilde{z})$  in a turbulent dataset called “T2” at  $Re = 1256$ ,  $\theta = 6^\circ \approx 3\alpha$  which shows considerable three-dimensionality. We notice that the along-duct flow  $\tilde{u}$  is about four times as strong as the other two components, except in the middle of the shear layer where turbulent fluctuations exceed the mean flow. Also,  $\tilde{v}$  is more energetic than  $\tilde{w}$ , which is typical of stratified turbulence because of the potential energy cost associated with vertical motions. We must keep in mind that the volume is not truly instantanenous as it is made of a sequence of  $\approx 40$  planes captured along  $\tilde{y}$  over a typical dimensionless time of  $O(1)$ . Hundreds of such volumes were typically captured by continuous back-and-forth scanning, providing time-resolved data over long times of  $O(10^2 - 10^3)$ , yielding  $\approx 150$  GB of raw data and  $\approx 3$  GB of processed data per experiment [43, 45].

A total of 16 such volumetric datasets spanning all flow regimes were used to build the energetics picture in Figure 5. To grasp how energy flows through the measured sub-volume (sketched in yellow), let us first consider the whole (closed) system composed of the duct (in red) and reservoirs (in grey). Initially, the presence of dense fluid on one side sitting above light fluid on the other side provides a large reservoir of “available” potential energy (Figure 5 (b)). An open duct allows this potential energy to be steadily converted into kinetic energy. Eventually, the fluids have been exchanged, the kinetic energy has been dissipated, some mixing has occurred in the process, and the system comes to rest. In the final state, the “available” potential energy has been transferred to internal energy, i.e. heat and “background” potential energy, that cannot drive any further motion [46]. We are interested in the energy fluxes (bottom sketch) during the statistically-steady state where potential energy is converted to kinetic energy and to heat. The GAFD community is particularly interested in the mixing efficiency  $\Gamma$ , the ratio of irreversible mixing to viscous dissipation, in other words the “tax” imposed by stratification on turbulence [3].

The measured sub-volume is bounded by four walls, but remains open and exchanges energy with the in-flow and out-flow along  $x$  (see yellow energy reservoir in Figure 5 (c)). When the flow is forced ( $\theta > \alpha$ ), the interface is approximately horizontal, the flow is approximately periodic in  $x$ , and these fluxes simplify as sketched, with a single external forcing  $F$  [47]. Essentially, the dimensionless kinetic energy reservoir  $\langle |\tilde{\mathbf{u}}|^2 / 2 \rangle_{x,y,z,t}$  is fed with an average flux  $\tilde{F} \approx 0.5 Ri_e Q_m \theta \approx 0.5 \times 0.15 \times 0.5 \times \theta \approx 0.04\theta$  (in radians). (Note that this and the following relations were derived for the turbulent “shear layer volume” highlighted by black lines in Figure 4 (b)), excluding laminar flow in the vicinity of the four walls [27, 48]). This flux feeds the mean kinetic energy (defined with respect to the  $x - t$  averaged velocity) and is balanced by the mean dissipation  $D$ . The key observation, supported by the experimental data [47, 48], is that the “hydraulic control” plateau in  $Q_m = 0.5$  enforces a plateau on the mean-flow dissipation  $D$ . The increase in  $F$  beyond this plateau in  $D$  opens another pathway, the production of turbulent kinetic energy (TKE)  $P$ , in order to close the kinetic energy budget. This production term is balanced by the TKE dissipation  $\varepsilon$ , and by a (weaker) buoyancy flux  $B$ , an inevitable consequence of vertical motions in a stratified flow (the potential energy cost). The budget of potential energy, approximately equal to the scalar variance  $(1/2) Ri_e \langle \tilde{\rho}^2 \rangle$ , is simple: the net production  $B$  is balanced by dissipation  $\chi$ , such that the average mixing efficiency is  $\Gamma = B/\varepsilon \approx \chi/\varepsilon$ . The limited experimental data suggest a modest tax of  $\Gamma \approx 0.05 - 0.1$  [48] (we return to it in Sec. 4.3). In a very turbulent flow where  $\varepsilon \gg D$ , the TKE dissipation is thus in direct balance with the forcing. In dimensionless units:

$$\tilde{\varepsilon} \approx \tilde{P} - \tilde{B} \approx \tilde{P}(1 - \Gamma) \approx \tilde{F}(1 - \Gamma) \approx 0.5 Q_m Ri_e \theta (1 - \Gamma) \approx 0.035\theta \quad (\text{in radians}). \quad (6)$$

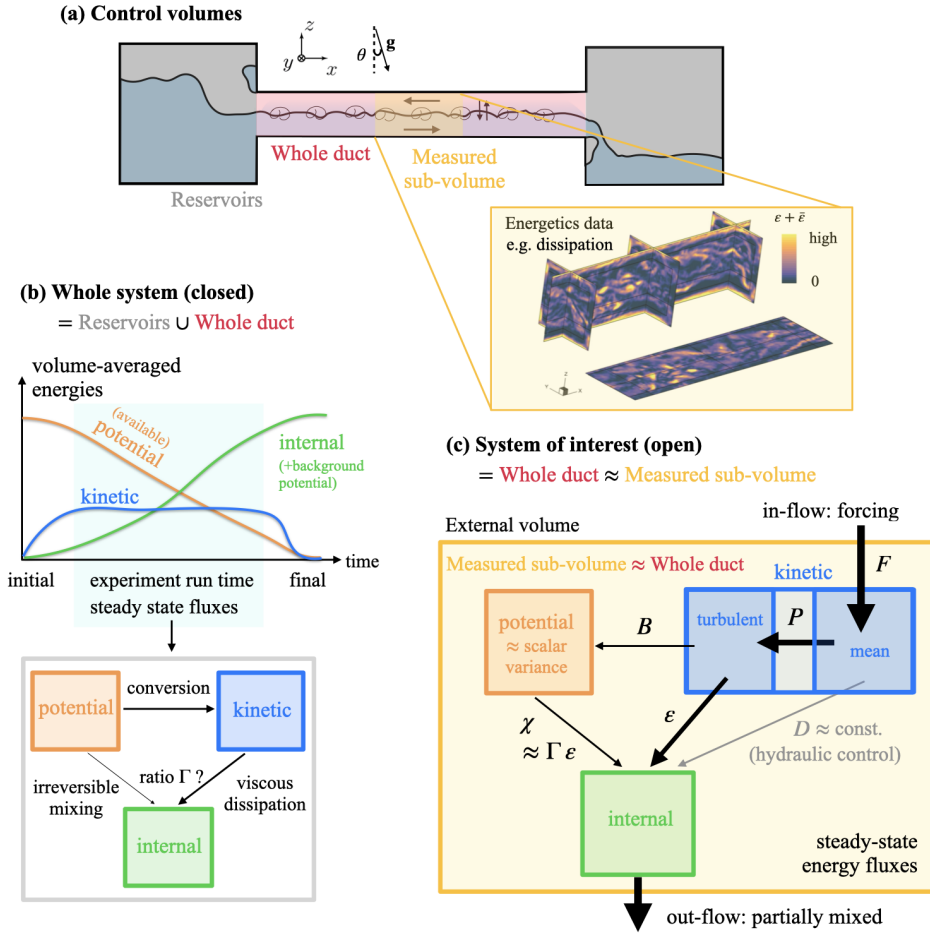


**Figure 5.** Energetics of SID, considering (a) control volumes, (b) the closed system (reservoir and duct) to provide background, and (c) the open system of interest (measured sub-volume of the duct, as in Figure 4). The out-of-equilibrium, statistically steady turbulence is forced by a flux  $F$  proportional to the tilt  $\theta$ . Under hydraulic control when  $\theta > \alpha$  (see Figure 3), [47, 48] showed that this flux is almost entirely dissipated turbulently by  $\varepsilon$ , leading to the keystone of SID turbulence (6).

This equation is the keystone of SID turbulence, and is firmly rooted in the data averaged over the turbulent shear layer volume. The second approximation assumes  $B/P \approx B/\varepsilon = \Gamma$  based on the observation that  $\Gamma \ll 1$ . The third approximation assumes  $\varepsilon \gg D$  which is expected by hydraulic control and supported by our moderately turbulent data. The last two approximations use our measured values for the key diagnostic flow parameters  $Q_m, Ri_e, \Gamma$ . Note that these values are expected to vary a little under a wider range of flow conditions  $Re, \theta, Pr$  than investigated so far, effectively modulating the prefactor in (6). The keystone equation  $\tilde{\varepsilon} \approx 0.035\theta$  is the quantitative energetic translation of the hydraulic arguments of Sec. 3.2. Beyond the state of hydraulic control, the baroclinic production of shear by the tilt  $\theta$  is balanced by interfacial dissipation  $\tilde{\varepsilon}$  (plus a modest mixing “tax”), keeping the interface in a marginal state of zero slope along the duct.

To wrap up this section on “first-order” findings, how does this keystone equation quantitatively explain the scaling of regime transitions with  $Re \theta$ ? Recalling that the TKE dissipation is

defined by the square norm of the turbulent strain rate tensor  $\tilde{\epsilon} = (2/Re)\|\tilde{\mathcal{S}}'\|^2$ , we deduce that  $\|\tilde{\mathcal{S}}'\|^2 \approx 0.02 Re\theta$  [47, 48]. In other words, the product  $Re\theta$  controls turbulence levels because an increase in the volume-averaged dimensionless turbulent strain rate must be achieved by vortex stretching and a cascade of energy to increasingly finer scales.

## 4. Second-order findings and open questions

### 4.1. *Instability, waves, coherent structures and transitions to turbulence*

How exactly does the stable, laminar exchange flow in SID become turbulent? Instability theory seeks to predict the onset of instability, the physical mechanism at play, and the resulting spatio-temporal flow structures. As a dimensionless parameter is varied, say  $Re$ , we know that the transition to turbulence can be either of “supercritical” or “subcritical” nature. The supercritical scenario, for example in Rayleigh–Bénard convection or Taylor–Couette flow dominated by inner-cylinder rotation, starts with a linear instability triggered by virtually any infinitesimal disturbance, followed by secondary instabilities in a gradual cascade leading to chaos and turbulence [49]. This scenario is fundamentally different to the subcritical scenario, for example in unidirectional pipe flow or plane Couette flow, which are linearly stable and thus require particular finite-amplitude disturbances. (Note that “supercritical” and “subcritical” have a different meaning here compared to the discussion on interfacial waves in Sec. 3.2). Turbulence, then, is akin to an abrupt phase transition, where turbulent regions compete with laminar regions and proliferate with a lifetime increasing with  $Re$  [50]. In SID, the repeatable onset of a Holmboe wave regime for a threshold in  $Re$  and  $\theta$ , the robustness of this regime in a wide region of  $(Re, \theta)$ , and the gradual increase in disorder at higher  $Re$ , are strong evidence of a supercritical scenario. Reynolds already understood in 1883 [17] that the transition to regular waves and turbulence in the exchange flow of Figure 1 (a) had, unlike in unidirectional flow, a critical velocity and was insensitive to the magnitude of perturbations, in other words, that it is supercritical.

What is causing the primary instability in SID? A necessary condition for the linear instability of an idealised stratified parallel shear flow is that the gradient Richardson number  $Ri_g(z) = N^2/S^2$  drops below the Miles–Howard criterion of  $1/4$  for some  $z$  [51]. In SID, because  $Pr \gg 1$ , a sharp density interface at  $z \approx 0$  is embedded within a more diffuse shear layer. This produces two local minima of  $Ri_g$  on either side of the interface, and thus the potential for an instability depending on the value of  $Ri_g$ . As  $Re\theta$  increases, the mass flux  $Q_m$  and thus the interfacial shear  $S$  increase while  $N$  remains unchanged, leading to a decrease of these  $Ri_g$  minima below  $1/4$  consistent with the observed onset of instability. This picture was confirmed with a stability analysis on the experimentally measured mean flow profiles, predicting growth at the correct wavelength and phase speeds [24]. As the density interface is sharp (recall  $Pr = 700$  with salt) and the stratification is significant (recall the bulk  $Ri = 1/4$ ) the instability in SID is not of Kelvin–Helmholtz type (which is stabilised by stratification) but instead of Holmboe type (which is destabilised by stratification), caused by the resonance of an internal gravity wave with the vorticity waves sandwiching it [52]. In this supercritical Holmboe transition (a pitchfork bifurcation), nonlinearities have a stabilising effect and eventually saturate the exponentially-growing instability [53] to a finite, observable amplitude as shown in Figure 2 (c)). Excellent agreement was indeed found between the measured three-dimensional Holmboe waves structure and the most unstable eigenfunctions predicted by the stability analysis performed on the two-dimensional ( $y-z$ ) mean flow [24]. This not only proved that the Holmboe waves in SID were saturated Holmboe instabilities, but also that they were distinctively three-dimensional because of confinement by the duct walls, most notably the side walls [54].

How do primary Holmboe waves eventually become turbulent? At  $Re = O(10^2)$  Holmboe waves travel as two modes of counter-rotating vortices on either side of a cusped density interface

(see Figure 2(c)), downward pointing triangle). Around  $Re = O(10^3)$ , secondary instabilities develop (see Figure 2(c)), upward pointing triangle). The occasional ejection of whisps creates only minimal mixing; instead it “scours” the the density interface and keeps it sharp [55]. This leads to a long-lived state of coherent Holmboe wave “turbulence”, which can be found up to  $Re = O(10^4)$  for zero or even slightly negative  $\theta$  [25]. Holmboe wave turbulence has been proposed to interpret field data in the deep ocean [56], surface ocean [57], and in an estuary [58] either through direct observation of its distinctive cusps or more indirect scouring behaviour. This turbulence differs markedly from the transient, rapidly overturning and less coherent turbulence resulting from the Kelvin–Helmholtz (K-H) transition found at lower  $Ri$  [59]. (Note that this K-H transition has also been achieved in SID by impulsively tilting the apparatus to a higher  $\theta$ , as in Thorpe’s experiment sketched in figure 1b. This allows to transiently exceeds the maximal exchange condition, thereby decreasing  $Ri$  below the hydraulic constraint of “steady SID”.)

How does SID flow become intermittently turbulent? Eventually, the Holmboe regime is replaced by the intermittent regime at  $Re = O(10^4)$  or at much lower  $Re$  if the tilt is  $0 < \theta < \alpha$ . What is the role of  $\theta$  in this further transition, which is defined by stronger interfacial overturning and mixing distinct from the spatio-temporal Holmboe coherence? In Sec. 3.2, we saw that turbulence levels were  $\propto Re\theta$  following an internal hydraulic jump, i.e., the instability of a shallow water wave of length comparable to the duct length (equivalently, the long-wave cousin of K-H, bounded by top and bottom walls [41]). This long-wave instability distorts the mean flow and leads to secondary, overturning instabilities of shorter wavelength comparable to the duct height, reminiscent of K-H billows. This hydraulic transition primarily caused by the ratio  $\theta/\alpha$  is clearly distinct from the Holmboe transition, but it is also of supercritical nature. Moreover, this hydraulic transition does not rely on the Holmboe transition, as was confirmed by mapping the  $(Re, \theta)$  regime diagram at  $Pr = 7$  (rather than 700) using temperature stratification. Indeed, shadowgraphs [31] and DNS [40] revealed that the more diffuse density interface supported transient internal waves but not Holmboe waves, without affecting the robust hydraulic transition associated with long waves. The two key control parameters  $Re$  and  $\theta$  in SID thus give rise to at least two fundamentally different and co-existing supercritical transitions, and  $Pr$  further complicates the picture. The addition of  $\theta$  to the classic linear stability problem has been recently shown to add multiple new families of long-wave instabilities, some of which do not even rely on shear or are only expected in extremely long systems ( $A = O(10^2 - 10^3)$ ) [60]. Their relevance to SID – and generally to the route to stratified turbulence – remains to be assessed. Many insightful discoveries likely await those interested in completing the picture of the transition to turbulence in SID in the space spanned by  $Re, \theta, Pr$  as well as the aspect ratios  $A, B$  (without mentioning the bulk  $Ri$ , which, as we touched upon, can be transiently lowered by impulsively tilting the duct, leading to yet another supercritical transition).

Finally, is the fully turbulent regime “aware” of these turbulent transitions? In other words, do transitions still “matter” even in distant regions of parameter space? According to dynamical systems theory, the answer is yes. Turbulence is viewed as underpinned by a relatively low-dimensional attractor, with phase-space trajectories spending significant time near a relatively small “skeleton” of exact (but unstable) solutions of the Navier–Stokes equations [61, 62]. Periodic orbit theory seeks to predict turbulent coherence and statistics using a weighted average over these simple solutions [63], some of which are likely connected to linear instabilities [64]. The search for such a skeleton in three-dimensional, stratified turbulence at  $Re = O(10^3 - 10^4)$  would be a formidable computational task. To stimulate such future endeavours, tantalising experimental evidence for this skeleton is accumulating in the form of coherent structures. In [65], their morphology has been tracked in SID across increasingly turbulent volumetric datasets, showing how hairpin-like vortical structures are born around the strong three-dimensional shearing structures of confined Holmboe waves. These hairpins gradually strengthen with  $Re\theta$  and morph

into pairs of upward- and downward-pointing hairpins propagating in opposite directions on either side of the partially mixed layer. Their arched-up heads entrain and engulf unmixed blobs of fluid into the mixed layer, while their legs further stir the fluid laterally and vertically causing mixing. In [26], the data-driven mining of shadowgraphs revealed further complexity across the two-dimensional space  $(Re, \theta)$ . At equal values of “turbulent intensity”  $Re\theta$  (and thus of the turbulent strain rate tensor  $\|\bar{s}'\|^2$ ) the dynamics at higher  $Re$  and lower  $\theta$  organises around distinctly different structures than vice versa (compare the star and pentagon symbols in Figure 2 (c)). Investigation of the intermittent regime therefore appears key to flesh out the dynamical systems picture of SID turbulence, as we discuss next.

#### 4.2. Temporal intermittency and self-organisation

Do the multiple primary instabilities in SID lead to multiple types of intermittency? The intermittent dynamics in the reduced-order space of [26] indeed revealed at least two different routes to turbulence at equal  $Re\theta$ . At higher  $Re$  and lower  $\theta$  the flow cycles quasi-periodically between three clusters labelled “laminarising” (decaying) turbulence, “braided” turbulence and “granular” (strongly three-dimensional and incoherent) turbulence. At lower  $Re$  and higher  $\theta$  the cycles are just as regular but the “granular” turbulence phase is replaced by an “overturning” turbulence phase, having steep, two-dimensionally coherent billows. Intermittency thus appears to organise around at least two distinct “slow manifolds” [66] in different regions of  $(Re, \theta)$ , but further progress on such data-driven reduced-order modelling is needed. At high  $\theta$ , the cycles to “overturning” turbulence are consistent with repeated hydraulic transitions (long wave instability giving rise to short overturning waves), but the “laminarising” phase has a partially mixed layer which begs for a more complex three-layer hydraulics model. At low  $\theta$ , the cycles to “granular” turbulence also remain to be explained, especially as the persistent third layer precludes the Holmboe instability but allows others, including Taylor–Caulfield [67]. The role of the boundary layers on the top, bottom and side walls should also be investigated. Although SID data suggest the boundary layers are laminar until  $Re \approx 10^3$  they likely become turbulent before  $Re = O(10^4)$  (depending on the duct length  $A$ ), another transition which may complicate the analysis further.

How do the intermittent dynamics evolve between the wave and turbulent regime? Spatio-temporal  $z-t$  diagrams generated from shadowgraphs (Figure 6 (a)) show that regular Holmboe waves are present at  $Re = 706$  with a temporal spectrum peaking at a dimensionless period of  $\approx 25$  (Figure 6(b)). The Holmboe coherence gradually disappears at  $Re = 993$  and  $1356$  with growing mixing shown by darker shades of grey in the shadowgraph variance. The quasi-periodic cycles between laminarising and intense granular turbulence become recognisable at  $Re = 1853$  and remarkably clear at  $Re = 2294$  and  $2828$ , with a temporal spectrum peaking at  $\approx 100$ . This coherence gradually fades at  $Re = 3426$ , and disappears entirely just above this value (not shown here). The emergence of turbulent patches and their subsequent evolution into a complex spatio-temporal pattern with increasingly long-lived turbulent events is reminiscent of the competition between bistable laminar and turbulent phases characteristic of the subcritical bifurcation in pipe flow [50]. Could the fully-developed “ultimate” turbulent regime in SID be reached subcritically, like in other initially supercritical systems such as boundary layers and Rayleigh–Bénard [13]? Alternatively, could it be reached supercritically by a homoclinic bifurcation? Recognising that the turbulent bursts may be caused by a repeated linear shear instability, could we interpret them as noisy homoclinic pulses [68], i.e., near-periodic visits in phase space in the vicinity of the laminar unstable saddle point, followed by large turbulent excursions away from it?

What sets the period of these cycles also remains an open question (here  $\approx 100$  dimensionless time units). One candidate timescale is the average duct transit time  $\approx 2A = 80$  shear time scales,

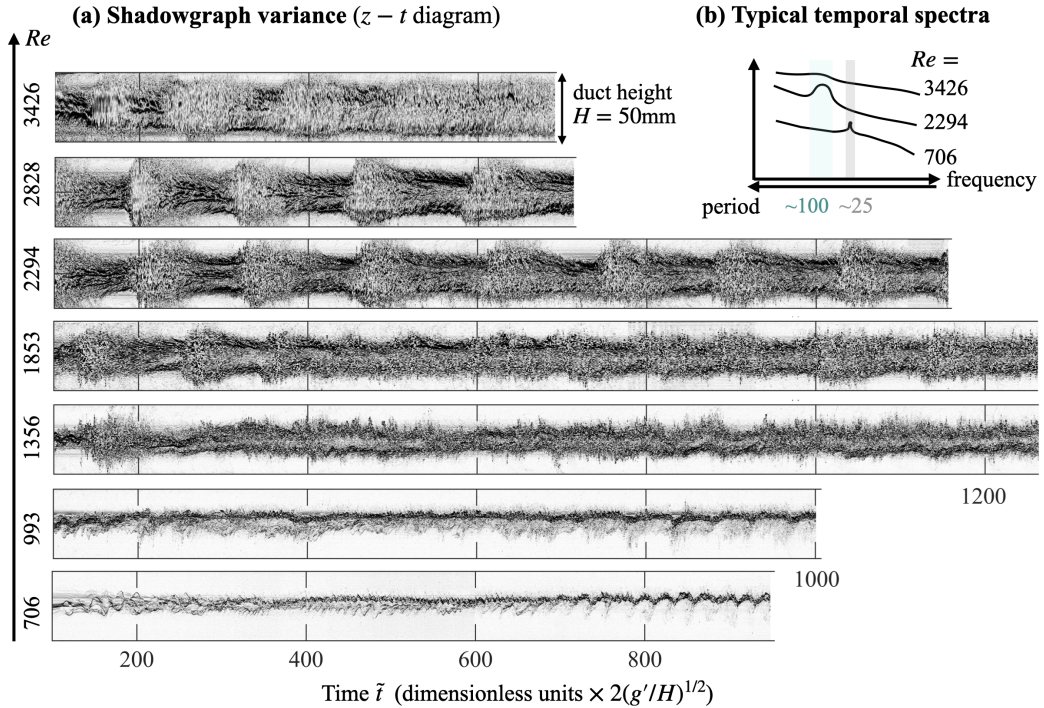


**Figure 6.** Intermittent turbulence evolving between the Holmboe wave regime at  $Re < 1000$  and the fully turbulent regime at  $Re > 3500$  (here  $\theta = 2^\circ \approx 1.4\alpha$ ). (a) Each spatio-temporal diagram show the temporal evolution of shadowgraph variance in a vertical slice across the full duct height. Darker shades indicate high shadowgraph variance caused by interfacial waves or turbulence. (Note we only show  $\tilde{t} > 100$  after the start of an experiment to discard initial gravity current transients.) The striking quasi-periodicity at intermediate  $Re$ , highlighted by idealised temporal spectra in (b), raises many open questions concerning the nature of the transitions to turbulence in SID (see Sec. 4.1-4.2).

taken by a fluid parcel travelling half the duct length at the layer-averaged speed  $\tilde{u} \approx Q_m \approx 0.5$ . Another candidate is the turbulent dissipation timescale (the ratio of TKE to  $\varepsilon$ ), which is an enigmatic  $\approx 10$  in the available turbulent data [48] (recall that the dimensionless shear timescale is 1 and the buoyancy timescale is 2). Cycles between turbulent de-stratification and quiescent re-stratification are common in geophysical applications, including in estuaries [69] and marginal seas [70] (controlled by tidal timescales) as well as the Pacific equatorial undercurrent [71] (controlled by diurnal solar heating). The “deep cycle” of equatorial ocean turbulence was explained by a low-dimensional interaction between mean shear and turbulence relying on the threshold  $Ri_g = 1/4$  [72], which may inspire a similar model for SID.

Finally, is intermittency the signature of an underlying universal turbulent equilibrium? Why does the flow dissipate a required flux in periodic turbulent bursts instead of in a continuous, but weaker turbulent equilibrium? This connects with the previous observation that fully-developed SID turbulence has a nearly uniform equilibrium gradient Richardson number  $Ri_g \approx Ri_e$  across the shear layer (see (5)). The idea of forced stratified turbulence being attracted to a constant  $Ri_e = O(0.1)$  was already clear to Turner in 1973 in his discussion of internal mixing processes [20, § 10.2] and connects to Monin–Obukhov similarity theory [73]. It was also interpreted in Holmboe wave turbulence [74] as a manifestation of self-organised criticality [75]. Self-organisation around  $Ri_e = 1/4$  is now central to the “marginal instability” paradigm for ocean turbulence [76, 77].



### 4.3. Turbulent parameterisations, length scales and spectra

A key objective in the GAFD community is to predict from a known ambient flow the unknown turbulent buoyancy flux  $B = \langle w' b' \rangle$  (previously sketched in Figure 5(c)), where  $b' = -g(\rho' - \rho_0)/\rho_0 = -(g'/2)\tilde{\rho}'$ . The simplest and most widely used parameterisation is the “flux-gradient” model,  $B = \kappa_T N^2$ , which posits that an unknown eddy diffusivity  $\kappa_T$  acts against the large-scale, stable gradient  $N^2 = \partial \langle b \rangle / \partial z = -(g'/H)\partial \langle \tilde{\rho} \rangle / \partial \tilde{z}$ , by analogy with the molecular flux  $\kappa N^2$ . The turbulent enhancement of buoyancy transport orders of magnitude above molecular values is quantified by the ratio

$$\frac{\kappa_T}{\kappa} = \frac{B}{\kappa N^2} = \frac{\nu}{\kappa} \frac{B}{\varepsilon} \frac{\varepsilon}{\nu N^2} = Pr \Gamma Re_b. \quad (7)$$

This key ratio is expressed as the product of three dimensionless parameters: the known Prandtl number  $Pr$  and the unknown (diagnostic) mixing efficiency  $\Gamma = B/\varepsilon$  introduced earlier, and the “buoyancy Reynolds number”

$$Re_b = \frac{\varepsilon}{\nu N^2} = Re \frac{\tilde{\varepsilon}}{\tilde{N}^2} \approx Ri_e^{-1} Re \tilde{\varepsilon} \approx 0.2 Re \theta. \quad (8)$$

In the above we used the observation that  $\tilde{N}^2 \approx Ri_e \approx 0.15$  (though  $Ri_e$  is expected to vary slightly with  $\delta$ , see (5)), and the keystone of SID turbulence for  $\tilde{\varepsilon}$  (see (6)). This key result connects the diagnostic  $Re_b$  in the shear layer to the prognostic  $Re \theta$ . In other words,  $\kappa_T/\kappa \approx 0.2 \Gamma Pr Re \theta$ , meaning that the key to unravel this mysterious ratio in SID lies in  $\Gamma$ .

What is the value of the mixing efficiency  $\Gamma$ ? This question has long been and remains debated [4, 78] given the leading role of  $\Gamma$  on the meridional overturning circulation of the ocean, and thus, on upwelling and downwelling rates [79]. More work is needed to understand why the canonical  $\Gamma = 0.2$  used by oceanographers appears robust in observations [4, 80, 81] despite theoretical arguments that  $\Gamma$  should vary substantially with the nature of the turbulence, including with  $Re_b$  and  $Pr$ . In SID, the experimental data at  $Re_b \approx 20$  and  $Pr = 700$  suggest  $\Gamma \approx 0.05 - 0.1$  [48] while the DNS data at  $Pr = 7$  suggest  $\Gamma = 0.1$  [40]. These values are two to three times below the value expected from parameterisations of  $\Gamma(Re_b)$  developed using transient K-H turbulence at  $Pr = 1$  [82]. Could these lower values of  $\Gamma$  in SID turbulence be due to the sustained forcing and much higher  $Pr$  [83]?

What does the important buoyancy Reynolds number  $Re_b$  represent? A scaling analysis of the Navier–Stokes equations reveals that in a stratified, anisotropic flow with a horizontal length scale  $L_h$  much larger than its vertical length scale, the vertical diffusion term is controlled not by  $Re$  but by  $Re_b = Re F_h^2$ , where  $F_h = U/(L_h N)$  is the horizontal Froude number [84]. Stratified turbulence requires not only a large  $Re$  and  $Re_b \gg 20$  but also a small  $F_h \ll 1$  to ensure the scalar remains active. This interpretation is consistent with the definition (8), i.e.  $Re_b = \varepsilon/(\nu N^2) \approx Re F_h^2$ , if we accept the inertial (unstratified) scaling  $\varepsilon \approx U^3/L_h$ . The requirement  $F_h \ll 1$  then ensures that a high  $Re_b$  is not achieved by a vanishing  $N^2$ . While this regime is notoriously difficult to achieve and sustain in DNS, (8) shows that it is surprisingly easy in SID. This is because stratification is always strong as  $F_h \approx (0.2\theta)^{1/2} \leq 0.2$  using our self-imposed bound  $\theta \leq 0.2$  rad  $\approx 11^\circ$ . The sustained production and dissipation of turbulence by  $\theta$  can thus access intense stratified turbulence  $Re_b = O(10^2 - 10^3)$  even at the modest laboratory scale of  $Re = O(10^4)$ . Furthermore, the community’s interpretation of  $Re_b$  as a turbulent intensity is fully consistent with the regimes transitions in SID, which are controlled by the volume-averaged turbulent strain rate tensor  $\|\tilde{\mathcal{S}}'\|^2 \approx 0.02 Re \theta \approx 0.1 Re_b$ .



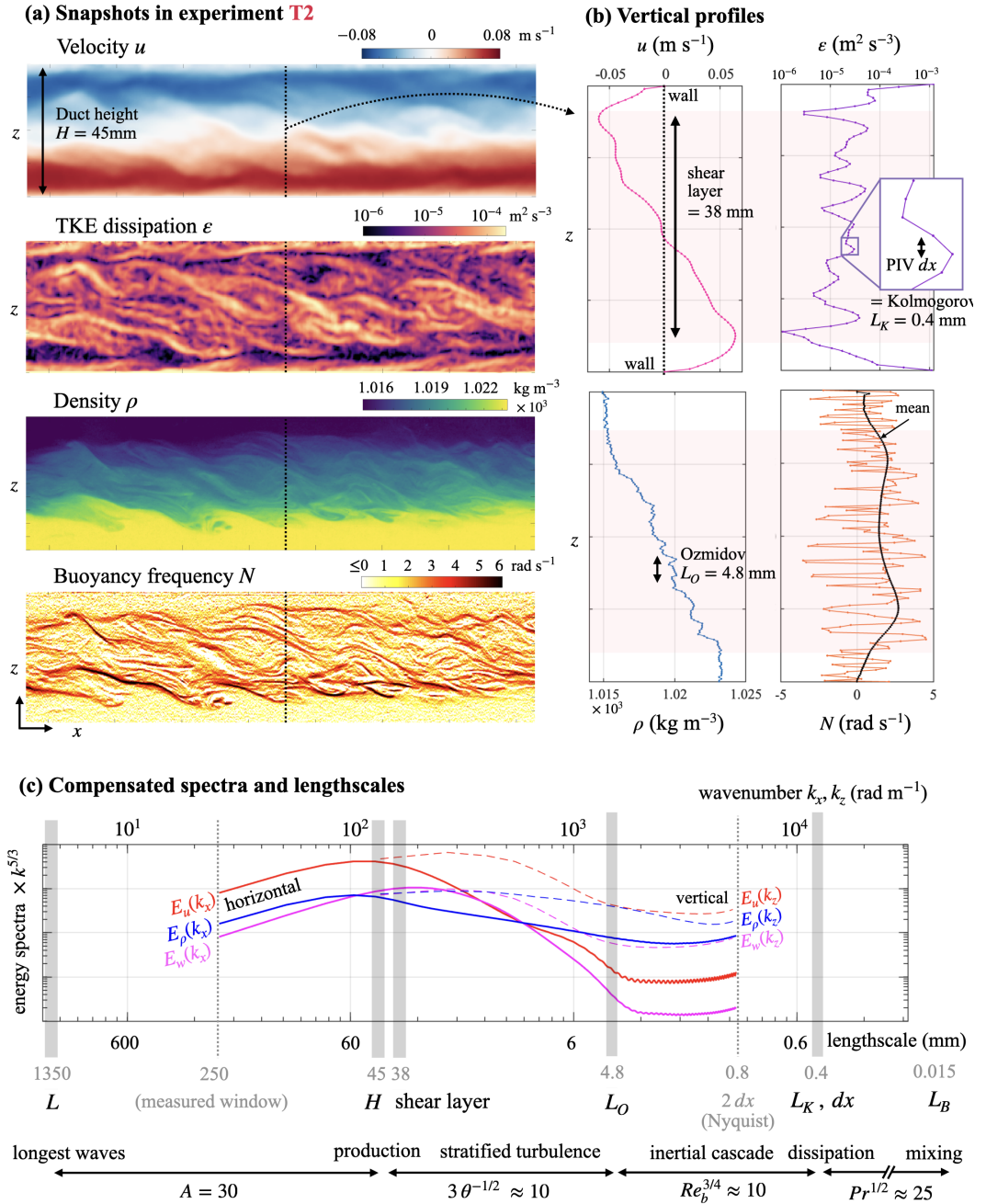


**Figure 7.** Fully-developed turbulence visualised by (a) two-dimensional snapshots, (b) one-dimensional profiles, and (c) energy spectra of  $u'$ ,  $w'$ ,  $\rho'$  demonstrating the hierarchy of length scales in dimensional units (see Sec. 4.3). We show the same T2 data as in Figure 4 at  $Re_b = 20$ . The data are shown without filtering, except  $\rho$ , which requires the raw LIF image to be filtered, and thus, down-sampled. Although the resolution of  $\rho$  still exceeds that of  $\mathbf{u}$ , energetics and spectra are computed here after collocating both on a grid of resolution  $dx$ , set by the PIV. The challenge of measuring turbulence at higher dynamic range  $Re_b$  is addressed in Sec. 5 and Figure 8.

What are the length scales of SID turbulence? It is useful to interpret  $Re_b$  as the ratio of the Ozmidov scale  $L_O$  to the Kolmogorov scale  $L_K$ :

$$Re_b = \left(\frac{L_O}{L_K}\right)^{4/3} \quad \text{where } L_O = \left(\frac{\varepsilon}{N^3}\right)^{1/2} \quad \text{and } L_K = \left(\frac{\nu^3}{\varepsilon}\right)^{1/4}, \quad (9)$$

Thus,  $Re_b$  is the dynamic range of scales that are neither affected by stratification ( $< L_O$ ) nor by viscous dissipation ( $> L_K$ ). To illustrate these scales in SID, Figure 7 (a) shows a snapshot of  $(u, \varepsilon, \rho, N)(x, z)$  in dimensional units and Figure 7 (b) shows corresponding vertical profiles using the T2 data at  $Re_b = 20$  (as previously shown in Figure 4). Black arrows indicate the important length scales in SID turbulence: the duct height  $H = 45$  mm, shear layer height 38 mm, the Ozmidov scale  $L_O = 4.8$  mm, and the Kolmogorov scale  $L_K = 0.4$  mm, which is here equal to the resolution of the PIV data  $dx$ .

The energy spectra in Figure 7 (c) help illustrate the separation between these scales (large to small from left to right). The compensated horizontal spectra of  $u$  (solid red),  $w$  (solid pink),  $\rho$  (solid blue) peak near the production scale  $H$ , before decaying in the stratified turbulence range until  $L_O$ , and plateauing in the inertia range towards  $L_K$  (the vertical spectra in dashed lines follow a similar trend). The plateau between  $L_O$  and  $L_K$  corresponds to a  $k^{-5/3}$  decay consistent with the classical Kolmogorov cascade expected in this range. However, this may be fortuitous, keeping in mind that spectra can suffer distortions at high wavenumbers due to the nature of PIV and the computation of Fourier transforms on non-periodic grided data [48]. Furthermore, the dynamical interpretation of scales defined in (8) should consider numerical prefactors which may be significant [85]. The dissipation range may in fact start at  $10L_K$  or above, in which case the T2 data shown in Figure 7 would be too viscous to even have an inertial range. These spectra also highlight the challenges of resolving scales below  $L_K$ , where at high  $Pr$  a broad viscous-convective subrange exists down to  $L_B = L_K Pr^{-1/2} = 15 \mu\text{m}$  here [86]. How do these microscopic scales feed back on the large scale flow and control layering and mixing efficiency [83]? We have shown in this section that SID is well suited to tackle stratified turbulence at high  $Re_b$  and  $Pr$ . In the next section, we explain how this could be achieved in the laboratory by future researchers.

## 5. The future: measuring geophysical stratified turbulence in the laboratory

### 5.1. Scaling up SID

Faced with the challenge of increasing the dynamic range  $Re_b$ , the SID experimenter must decide on three main parameters: the physical height of the duct  $H$  (units: m), the dimensionless density difference driving the flow  $\Delta$ , and the tilt of the apparatus  $\theta$ . Table 2 summarises how these three parameters control the scaling of the key SID variables. The peak flow speed in each layer is approximately  $U \approx (g'H)^{1/2} \approx 3.1 H^{1/2} \Delta^{1/2} \text{ m s}^{-1}$  (assuming a maximum mass flux  $Q_m \approx 0.5$ ). The dimensional translation of the keystone of SID turbulence for the time- and volume-averaged TKE dissipation within the shear layer (6) is  $\varepsilon \approx 0.035 \theta U^3 / (H/2) \approx 2.2 H^{1/2} \Delta^{3/2} \theta \text{ m}^2 \text{ s}^{-3}$  (or  $\text{W kg}^{-1}$ ). The buoyancy frequency scales with  $(g'/H)^{1/2}$  and we find an average  $N \approx 2.6 H^{-1/2} \Delta^{1/2}$  (the pre-factor varies across the shear layer between 1.0 – 4.5). The expressions for  $Re$ ,  $Re_b$ ,  $L_O$  and  $L_K$  follow from (1), (8) and (9). The separation of scale between the shear layer height  $H$ , the Ozmidov scale  $L_O$  and the Kolmogorov scale  $L_K$  are deduced as

$$\frac{H}{L_O} \approx 3 \theta^{-1/2}, \quad \frac{H}{L_K} \approx 3.8 \times 10^4 H^{9/8} \Delta^{3/8} \theta^{1/4}, \quad \frac{L_O}{L_K} \approx 1.3 \times 10^4 H^{9/8} \Delta^{3/8} \theta^{3/4}, \quad (10)$$

as sketched in Figure 8(a). Comparing with results from the previous section, we note that  $L_O/H \approx 0.7F_h$ , which is consistent with  $Re_b \approx 0.2 Re \theta \approx Re F_h^2$  and  $L_h \approx 0.7L_O$ .

**Table 2.** Key estimates for SID turbulence as functions of duct height  $H$  (in m), dimensionless density difference  $\Delta$ , and  $\theta$  (in radians). The flow speed  $U$  is the peak in each layer (used for  $Re$ ), while  $\varepsilon, N, Re_b, L_k$  and  $L_O$  are shear-layer averages.

Flow speed (layer peak)	$U$	$\approx 3.1 H^{1/2} \Delta^{1/2}$	$\text{m s}^{-1}$
TKE dissipation	$\varepsilon$	$\approx 2.2 H^{1/2} \Delta^{3/2} \theta$	$\text{m}^2 \text{s}^{-3}$
Buoyancy frequency	$N$	$\approx 2.6 H^{-1/2} \Delta^{1/2}$	$\text{rad s}^{-1}$
Reynolds number	$Re$	$\approx 1.6 \times 10^6 H^{3/2} \Delta^{1/2}$	–
Buoyancy Reynolds	$Re_b$	$\approx 3.1 \times 10^5 H^{3/2} \Delta^{1/2} \theta$	–
Ozmidov scale	$L_O$	$\approx 0.34 H \theta^{1/2}$	m
Kolmogorov scale	$L_K$	$\approx 2.6 \times 10^{-5} H^{-1/8} \Delta^{-3/8} \theta^{-1/4}$	m

The expressions for  $(\varepsilon, N)(H, \Delta, \theta)$  allow us to compare in Figure 8 (b) the “practical” SID region (in yellow) to geophysical stratified turbulence (in purple) [87, 88]. The yellow region is the two-dimensional projection of a cuboid whose sides are spanned by  $H, \Delta, \theta$  (see black arrows). The overlap in this diagram is remarkable as it shows that by varying these three simple parameters, SID can reproduce the low  $\varepsilon$  and  $N$  found, for example, in the deep ocean as well as the high  $\varepsilon$  and  $N$  found, for example, in the upper ocean and estuaries. Overlap in this dimensional space is, however, not necessary to tackle geophysical stratified turbulence; it is sufficient to achieve similitude in the dimensionless  $Re_b$ . By spanning nearly three orders of magnitude  $Re_b = O(10 - 10^4)$ , SID can be dynamically similar – and thus simulate – the vast majority of geophysical conditions. In fact, it remains to be seen if exploration well above  $Re_b = O(10^2)$  is necessary, as DNS suggest that an asymptotic state may be reached around  $Re_b = 300$  [89].

What values of  $Re$  and  $Re_b$  can the experimenter achieve? Figure 8 (c-d) illustrates their scaling in the  $(H, \Delta)$  plane, noting that we assumed for  $Re_b$  a modest tilt  $\theta = 0.1 \approx 6^\circ$  (as in the T2 data, shown by a red star). What determines the limits of the “practical SID region” in yellow? Practical considerations suggest that we keep the duct height  $0.05 \text{ m} \leq H \leq 0.5 \text{ m}$ , while the Boussinesq approximation and matching the refractive indices for PIV and LIF with NaCl/NaNO<sub>3</sub> salts suggest  $\Delta \leq 0.05$ . Using these maximum values, one can reach  $Re \approx 10^5$  and  $Re_b \approx 2000$ . Since  $Re_b \propto \theta$ , this value (and all  $Re_b$  contour values in Figure 8(d)) would be doubled for  $\theta = 0.2 \text{ rad} \approx 11^\circ$ , a suggested maximum for turbulence to remain nearly horizontal and thus stably stratified. Next, the choice of  $\theta$  is connected to the duct aspect ratio  $A$ , or equivalently, its geometrical slope  $\alpha \approx A^{-1}$ . Forced flow conditions with dissipation obeying (6) require a forcing parameter  $\theta/\alpha \geq 1$ , but keeping the mixed layer below 70 % of the duct height to avoid boundary effects requires  $\theta/\alpha \leq 3$  according to (3). These bounds suggest  $0.016 \leq \theta \leq 0.2$ , the minimum being achieved for  $\theta = \alpha = 1/60 \approx 1^\circ$  (for  $A = 60$ ) and the maximum  $\theta = 3\alpha = 3/15 \approx 11^\circ$  (for  $A = 15$ ). This effectively suggests that the duct should be long enough ( $A \geq 15$ ) but not too long ( $A \leq 60$ ) for the setup to remain practical and for  $\theta$  to remain measurable. Figure 8(e) shows how the  $(\theta/\alpha, A)$  space influences the separation of scale  $H/L_O$ . As  $H/L_O \approx 1.4F_h^{-1}$  the top left corner the yellow region ( $F_h \approx 0.2$ ) harbours less strongly stratified turbulence, and thus more large-scale density overturns [26, 27], than the bottom right corner ( $F_h \approx 0.06$ ).

In summary, geophysical values up to  $Re_b = O(10^3)$  can be reached in SID. Limiting ourselves for now to the goal of reaching  $Re_b = 300$  to test the hypothesis of an asymptotic behaviour [89], the green regions in Figure 8 (c-d) show that such values have already been achieved. Shadow-graph data exists up to  $Re = 200,000$  and  $Re_b = 300$  was achieved with  $H = 0.1 \text{ m}$  [16, 25, 33], while more recently  $Re_b = 100$  was achieved with a more modest  $H = 0.05 \text{ m}$  [26, 32]. Velocity measurements, however, do not yet exist at these high  $Re_b$ , not least because of the very large

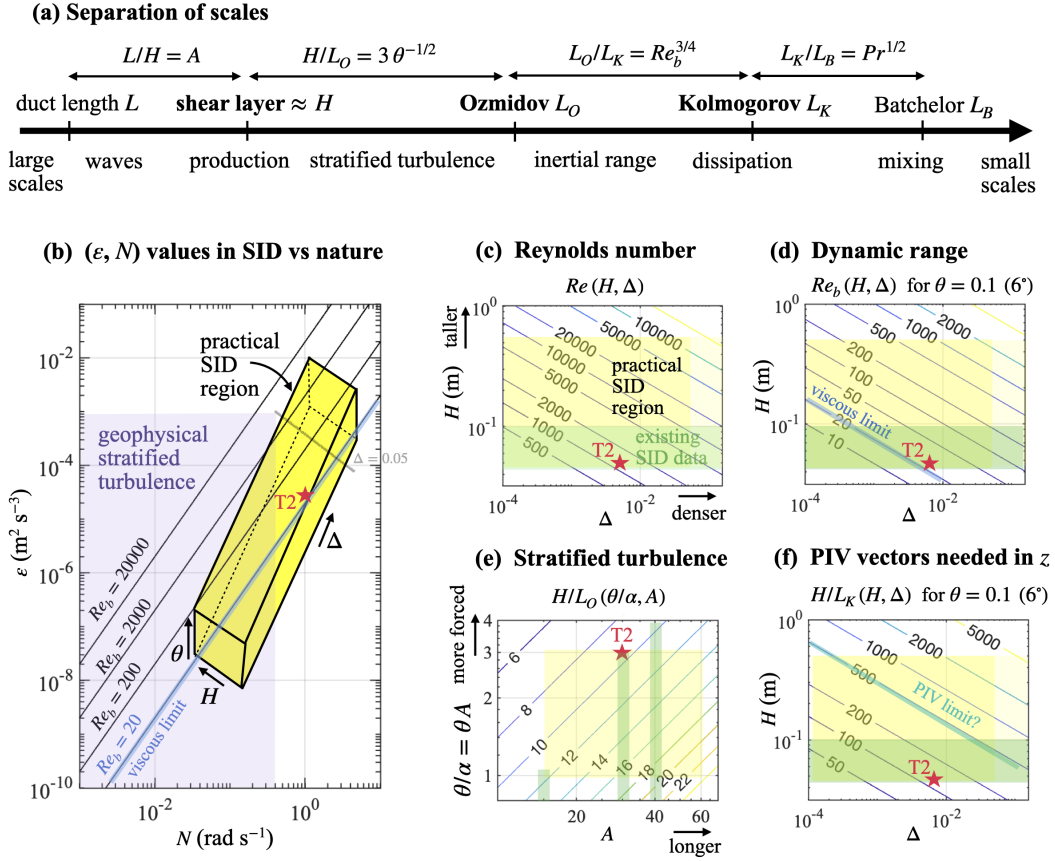


**Figure 8.** Geophysical stratified turbulence in the laboratory using SID (see Sec. 5). (a) The separation between scales is controlled by the dynamic range  $Re_b \approx 0.2 Re\theta$ , as well as  $A$ ,  $\theta$ , and  $Pr$ . (b) SID can access  $Re_b = O(10^3 - 10^4)$  (in yellow), with significant overlap in dimensional  $(\varepsilon, N)$  in strongly stratified (high  $N$ ) geophysical flows. The arrows on the sides of the yellow “practical SID region” cuboid show the effect of increasing the duct height  $H$ , density difference  $\Delta$  and tilt  $\theta$  within the practical bounds discussed in the main text  $H \in [0.05\text{m}, 0.5\text{m}]$ ,  $\Delta \in [0.0001, 0.15]$  (or 0.05, annotated in grey, to satisfy Boussinesq and match refractive indices), and  $\theta \in [1^\circ, 11^\circ]$ . The scaling of (c)  $Re$ , (d)  $Re_b$  with  $H$  and  $\Delta$  show that  $Re_b = O(10^3)$  may be obtained at relatively modest laboratory values of  $Re = O(10^5)$  thanks to  $\theta$ , according to (8). The scaling of (e)  $H/L_O(\theta/\alpha, A)$  shows how the tilt  $\theta$  and the duct aspect ratio  $A$  influence the nature of stratified turbulence, while (f)  $H/L_K(\Delta, H)$  shows the required resolution of PIV measurements, which controls the design of future experiments.

separation of scale  $H/L_K$  and the required PIV resolution (see Figure 8 (f)). Next, we discuss how to make them a reality.

## 5.2. Experimental design and technological challenges

What makes accurate PIV and LIF measurements so challenging at high  $Re_b$ ? How should future SID experiments be designed to achieve a new milestone at  $Re_b = 300$ ? (This would be over an order of magnitude above the T2 data at  $Re_b = 20$  shown in Figures 4 and 7.)

First, we need to choose the duct height, which, according to table 2, is  $H \approx 2.2 \times 10^{-4} Re_b^{2/3} \Delta^{-1/3} \theta^{-2/3}$  (in m). Achieving  $Re_b = 300$  under the constraints  $\Delta \leq 0.05$  and  $\theta \leq 0.2$  requires a minimum height  $H \geq 80$  mm, as well as  $Re \approx 5 Re_b \theta^{-1} \geq 8000$  and  $H/L_K \approx 2.9 Re_b^{3/4} \theta^{-1/2} \geq 500$ . These minimum values assume the maximum  $\theta = 0.2 = 3\alpha$  with the minimum aspect ratio  $A = 15$ , and they would all increase for a lower  $\theta$  or higher  $A$ . Can we select the minimum height of  $H = 80$  mm to keep the apparatus as compact as possible? Unfortunately not, because it would be too small for PIV. The reason is that a distinct pattern of particles in each interrogation window suggests a minimum vector spacing of  $dx \geq 500 \mu\text{m}$ , considering that particles should have a diameter  $\geq 30 \mu\text{m}$  due to limits on the particle seeding density and the diffraction of visible light. Furthermore, we wish to resolve the Kolmogorov scale, i.e.  $dx = L_K$ , to obtain velocity spectra accurate down to a scale no smaller than  $\approx 5L_K$  (because of the Nyquist cut-off and high-wavenumber filtering artefacts inherent to PIV and Fourier transforms [48]). As a result, the duct height must be scaled up to a minimum height of  $H = 500 L_K = 500 dx = 250$  mm and length of  $L = AH = 3.75$  m. Conveniently, this larger scale allows us to achieve our target  $Re_b = 300$  and  $Re = 8000$  with a lower  $\Delta \approx 0.0015$  (which is more forgiving for matching refractive indices) and slower velocity  $U$  (and thus a better “freezing” of the flow by scanning).

Does the camera hardware impose further constraints? Not substantially. Using PIV interrogation windows that are a minimum of 20 pixels wide and a vector spacing of 10 pixels (50 % overlap between windows), resolving the separation of scale  $H/L_K = H/dx = 500$  along  $z$  requires 5000 pixels, which around the current limit of high-speed cameras (note that the aspect ratio of the image would limit the extent of the domain along  $x$ ). Even in an ideal world where LIF would output a meaningful density data point per pixel, we will likely never resolve the separation of scales  $H/L_B \approx 500 Pr^{1/2} \approx 13,000$ . In reality, the LIF signal is not expected to be at a much higher usable resolution than the PIV signal because filtering is almost always required to eliminate various sources of high-frequency noise in the dye intensity signal, which is why it is often collocated on the PIV grid. Numerical data assimilation is a promising direction to super-resolve the flow between  $L_K = 500 \mu\text{m}$  and  $L_B = 20 \mu\text{m}$ . Physics-informed neural networks can achieve this without having to simulate the flow (which would be prohibitively expensive) as was shown in SID [90]. However, strongly turbulent flows pose convergence and implementation challenges which future research will hopefully resolve.

Next, what scanning and laser frequencies are required to reconstruct quasi-instantaneous three-dimensional volumes? To scan the duct width in an ambitious dimensionless time of 0.4, the traversing speed should be  $5BU \approx 300 \text{ mm s}^{-1}$  assuming a square duct  $B = 1$ . To ensure that at least 90% of the time is spent scanning the volume at constant speed, each ramp-up and ramp-down phases on either end of the volume should have an acceleration of at least  $\approx 500 B g' \approx 0.75g$  with adequate vibration control. To fit  $n_y = 200$  planes across  $y$  (with a spacing of 2.5 mm typical of the thickness of a laser sheet), the frequency of the dual-cavity pulsed laser should be  $5n_y(g'/H)^{1/2} = 250$  Hz (note the scaling with the buoyancy frequency). As far as video recording is concerned, this setup would output a typical 250 pairs of  $5 \times 5 = 25$  MPixels raw images per second per camera (assuming a square image). Assuming an 8-bit depth suitable for PIV (but limiting for LIF) this would require a bandwidth of  $100 \text{ Gbit s}^{-1} = 12.5 \text{ GB s}^{-1}$  per camera. This precisely matches the best 100 Gigabit Ethernet networking technology, but it exceeds the current speed of solid state drives. Progress on computing hardware is thus needed to match the desired scanning speed. Parallelised PIV post-processing is also required (now standard in the DigiFlow software [44]), and would output volumes of  $500 \times 200 \times 500 = 5 \times 10^8$  vectors in  $(x, y, z)$ .

What reservoirs are needed on either side of the duct? Here a generous rule of thumb is to sustain a layer-averaged exchange flow rate of  $(U/2)BH^2/2$  during five duct transit times  $5AH/(U/2) \approx 625$  s for the turbulent dynamics to be in quasi-equilibrium (corresponding to  $20A = 300$  shear time scales). Each reservoir should therefore have a volume  $5ABH^3 \approx 1.2 \text{ m}^3$ ,

i.e., twice the exchanged volume, assuming the duct connects at mid-level in both reservoirs and neglecting mixing. (Note this volume will increase if the experimenter chooses  $B > 1$  to reduce the influence of side walls.) Finally, how much salt should be dissolved in each reservoir? Achieving the density difference  $\Delta$  at a matched refractive index would require concentrations of  $\approx 0.8$  wt %  $\text{NaNO}_3$  and  $\approx 0.5$  wt %  $\text{NaCl}$  corresponding to a modest  $\approx 10$  kg and  $\approx 6$  kg of dry salt, respectively.

Other challenges are worth highlighting. First, this experiment would generate at least  $\approx 3 \times 12.5 \text{ GB/s} \times 625 \text{ s} \approx 23 \text{ TB}$  of raw data. Although the processed data would be more compact, data transfer, storage and back up resources become a key issue. Post-processing times are also expected to increase, perhaps from a few days to a few weeks per experiment. Second, the time needed for the preparation and acquisition of experiments, often by a pair of experimentalists, depends on the size of the reservoirs and other design details. This time ranged from one or two days per experiment with the “second generation” apparatus (see Sec. 2.2) having reservoirs of volume  $\sim 0.08 \text{ m}^3$  each and an easily-accessible 1.35 m-long duct thanks to open-lid reservoirs, to several days with the “third generation” apparatus having reservoirs of volume  $\sim 0.4 \text{ m}^3$  each and a less accessible 2 m-long duct because of closed lids. The advanced nature of the imaging also requires much trial and error; not all experiments yield usable data.

In summary, these guidelines illustrate how PIV imaging at the small Kolmogorov scales at high  $Re_b$  imposes a minimum duct height  $H$  controlling the overall design of SID experiments. The greatest challenge lies in the acquisition of near-instantaneous volumetric data, particularly because of the required scanning and recording speed. Relaxation of a few specifications, ingenious workarounds and technological progress will allow future researchers to get very valuable data at  $Re_b = O(10^2)$ .

## 6. Conclusions

In conclusion, the Stratified Inclined Duct (SID, see Sec. 2) is a conceptually simple laboratory experiment that allows us to control and measure shear-driven, stably-stratified turbulence with the necessary and sufficient realism and complexity needed to drive substantial progress in geophysical and astrophysical fluid dynamics (GAFD). This paper focused on transition and mixing, which are two theoretical and practical questions central to GAFD.

When turbulence sets in, the transition is often mediated by internal or interfacial waves and shear instabilities, which control where and when turbulence grows, persists, or decays. In SID, the multi-dimensional parameter space spanned by the Reynolds number  $Re$ , the tilt angle  $\theta$  and the Prandtl number  $Pr$  gives rise to a variety of flow regimes and transitional states between them. Successive generations of measurements, including shadowgraph data (Sec. 3.1), mass flux data (Sec. 3.2), and fully-resolved three-dimensional velocity and density data (Sec. 3.3), recently assisted by direct numerical simulations (DNS), discovered multiple supercritical bifurcations, but also raised a multitude of questions, in particular on the ultimate route to chaos (Sec. 4.1). The dynamical systems “skeleton” of high- $Re$  and high- $Pr$  turbulence, both in geophysics and in SID, is intimately connected to spatio-temporal intermittency, layering and self-organising equilibria, on which much remains to be discovered (Sec. 4.2).

When turbulence intensifies, small-scale mixing vastly enhances the transport of the buoyancy (heat, salt) and other scalars, with leading-order feedbacks and implications on the large-scale flows such as those controlling Earth’s climate. The effects of mixing are captured by parameterisations, typically using the eddy diffusivity in (7). A key challenge lies in understanding how the mixing efficiency  $\Gamma$  scales with  $Pr$  and with the turbulent intensity called the buoyancy Reynolds number  $Re_b$ , which is also a key separation of scales (Sec. 4.3). In SID, the continuous baroclinic generation of sheared turbulence by a sufficiently large tilt of the duct is balanced by the dissipation, in an equilibrium distilled in the “keystone” equation (6). SID thus offers the rare

ability to control and sweep through  $Re_b$  with the simple product  $Re\theta$  (see (8)), thereby accessing values of  $Re_b = O(10 - 10^3)$  relevant to most geophysical turbulence and allowing us to extrapolate laboratory results. Practical design guidelines should assist future efforts to scale SID up (Sec. 5.1) and overcome spatial resolution challenges (Sec. 5.2) to measure the full flow field at  $Re_b = 300$ . This is an order of magnitude above current values and would be a new decisive milestone for the community.

Experimental data outputs are now converging with what would be expected from DNS, which remain extremely costly and challenging in this parameter regime. Data assimilation offers exciting prospects to accelerate this convergence. DNS of sufficiently real and complex flows inspired and validated by laboratory experiments have been and will remain powerful and complementary tools. We hope this paper may inspire future combined experimental and numerical investigations of SID, and mobilise the collective expertise of the community needed to unravel the intricacies of geophysical stratified turbulence.

## Acknowledgements

I am deeply grateful to P. F. Linden for the opportunity to work on this fascinating problem and for his invaluable mentorship. I am also indebted to S. B. Dalziel, who conceived the volumetric scanning technique, and to J. L. Partridge, X. Jiang, G. Kong and the technicians of the G. K. Batchelor Laboratory for their precious experimental expertise and support. This paper is enriched by the collaborations and discussions I have been fortunate to have over the years, particularly with the stratified turbulence group in DAMTP. Finally, I acknowledge support from the 2023 GFD program at the Woods Hole Oceanographic Institution and discussions that contributed to this paper, including with S. M. de Bruyn Kops, C. P. Caulfield, T. S. Eaves, W. R. Geyer, D. Lohse, J. J. Riley and B. R. Sutherland.

## Declaration of interests

The author does not work for, advise, own shares in, or receive funds from any organisation that could benefit from this article, and have declared no affiliation other than their research organisations

## References

- [1] E. A. D'Asaro, "How do Internal Waves Create Turbulence and Mixing in the Ocean?", 2022. Preprint, ESS Open Archive.
- [2] A. V. Melet, R. Hallberg and D. P. Marshall, "The role of ocean mixing in the climate system", in *Ocean Mixing. Drivers, Mechanisms and Impacts*, Elsevier, 2022, pp. 5–34.
- [3] C. P. Caulfield, "Open questions in turbulent stratified mixing: Do we even know what we do not know?", *Phys. Rev. Fluids* **5** (2020), article no. 110518.
- [4] M. C. Gregg, E. A. D'Asaro, J. J. Riley and E. Kunze, "Mixing efficiency in the ocean", *Ann. Rev. Mar. Sci.* **10** (2018), pp. 443–473.
- [5] T. Dauxois et al., "Confronting Grand Challenges in environmental fluid mechanics", *Phys. Rev. Fluids* **6** (2021), no. 2, article no. 020501.
- [6] B. R. Sutherland, *Internal Gravity Waves*, Cambridge University Press, 2010.
- [7] C. P. Caulfield, "Layering, instabilities, and mixing in turbulent stratified flows", *Ann. Rev. Fluid Mech.* **53** (2021), pp. 113–145.
- [8] W. D. Smyth and J. N. Moum, "Length scales of turbulence in stably stratified mixing layers", *Phys. Fluids* **12** (2000), no. 6, pp. 1327–1342.
- [9] P. Bartello and S. M. Tobias, "Sensitivity of stratified turbulence to the buoyancy Reynolds number", *J. Fluid Mech.* **725** (2013), pp. 1–22.

- [10] S. Almalkie and S. M. De Bruyn Kops, “Kinetic energy dynamics in forced, homogeneous, and axisymmetric stably stratified turbulence”, *J. Turbul.* **13** (2012), article no. N29.
- [11] M. M. P. Couchman, S. M. de Bruyn Kops and C. P. Caulfield, “Mixing across stable density interfaces in forced stratified turbulence”, *J. Fluid Mech.* **961** (2023), article no. A20.
- [12] M. Avila, D. Barkley and B. Hof, “Transition to Turbulence in Pipe Flow”, *Ann. Rev. Fluid Mech.* **55** (2023), pp. 575–602.
- [13] D. Lohse and O. Shishkina, “Ultimate turbulent thermal convection”, *Phys. Today* **76** (2023), no. 11, pp. 26–32.
- [14] D. Feldmann, D. Borrero-Echeverry, M. J. J. Burin, K. Avila and M. Avila, “Routes to turbulence in Taylor–Couette flow”, *Philos. Trans. R. Soc. Lond., Ser. A* **381** (2023), no. 2246, article no. 20220114.
- [15] D. Lohse, “Causality in Rayleigh–Bénard and Taylor–Couette turbulence”, in *Caust Workshop on Causality in Turbulence and Transition*, 2022.
- [16] C. R. Meyer and P. F. Linden, “Stratified shear flow: experiments in an inclined duct”, *J. Fluid Mech.* **753** (2014), pp. 242–253.
- [17] O. Reynolds, “An experimental investigation of the circumstances which determine whether the motion of water shall be direct or sinuous, and of the law of resistance in parallel channels”, *Philos. Trans. R. Soc. Lond.* **174** (1883), pp. 935–982.
- [18] S. A. Thorpe, “Experiments on the instability of stratified shear flows: miscible fluids”, *J. Fluid Mech.* **46** (1971), no. 02, pp. 299–319.
- [19] E. O. Macagno and H. Rouse, “Interfacial mixing in stratified flow”, *J. Eng. Mech.* **87** (1961), no. 5, pp. 55–81.
- [20] J. S. Turner, *Buoyancy effects in fluids*, Cambridge University Press, 1973.
- [21] G. I. Taylor, “An Experiment on the Stability of Superposed Streams of Fluid”, *Math. Proc. Camb. Philos. Soc.* **23** (1927), no. 6, pp. 730–731.
- [22] E. J. Strang and H. J. S. Fernando, “Entrainment and mixing in stratified shear flows”, *J. Fluid Mech.* **428** (2001), pp. 349–386.
- [23] P. Odier, J. Chen and R. E. Ecke, “Entrainment and mixing in a laboratory model of oceanic overflow”, *J. Fluid Mech.* **746** (2014), pp. 498–535.
- [24] A. Lefauve, J. L. Partridge, Q. Zhou, C. P. Caulfield, S. B. Dalziel and P. F. Linden, “The structure and origin of confined Holmboe waves”, *J. Fluid Mech.* **848** (2018), pp. 508–544.
- [25] A. Lefauve and P. F. Linden, “Buoyancy-driven exchange flows in inclined ducts”, *J. Fluid Mech.* **893** (2020), article no. A2.
- [26] A. Lefauve and M. M. P. Couchman, “Data-driven classification of sheared stratified turbulence from experimental shadowgraphs”, *Phys. Rev. Fluids* **9** (2024), article no. 034603.
- [27] A. Lefauve and P. F. Linden, “Experimental properties of continuously forced, shear-driven, stratified turbulence. Part 1. Mean flows, self-organisation, turbulent fractions”, *J. Fluid Mech.* **937** (2022), article no. A34.
- [28] C. S. Ng, A. Ooi, D. Lohse and D. Chung, “Bulk scaling in wall-bounded and homogeneous vertical natural convection”, *J. Fluid Mech.* **841** (2018), pp. 825–850.
- [29] T. Maxworthy, “Experiments on gravity currents propagating down slopes. Part 2. The evolution of a fixed volume of fluid released from closed locks into a long, open channel”, *J. Fluid Mech.* **647** (2010), pp. 27–51.
- [30] Y. Tanino, F. Moisy and J.-P. Hulin, “Laminar-turbulent cycles in inclined lock-exchange flows”, *Phys. Rev. E* **85** (2012), no. 6, article no. 066308.
- [31] A. Lefauve, *Waves and turbulence in sustained stratified shear flows*, PhD thesis, University of Cambridge, Cambridge, United Kingdom, 2018.
- [32] X. Jiang, G. Kong and A. Lefauve, *Shadowgraph visualisations of salt-stratified turbulence obtained in a stratified inclined duct (SID) laboratory experiment*, dataset, Apollo - University of Cambridge Repository (December 14, 2023). <https://doi.org/10.17863/CAM.104471>, 2023.
- [33] A. Lefauve and P. F. Linden, *Research data supporting “Buoyancy-driven exchange flows in inclined ducts”*, dataset, Apollo - University of Cambridge Repository (April 17, 2020). <https://doi.org/10.17863/CAM.48821>, 2020.
- [34] D. E. Kiel, *Buoyancy driven counterflow and interfacial mixing*, PhD thesis, University of Cambridge, Cambridge, United Kingdom, 1991.
- [35] G. O. Hughes and P. F. Linden, “Mixing efficiency in run-down gravity currents”, *J. Fluid Mech.* **809** (2016), pp. 691–704.
- [36] J. B. Schijf and J. C. Schönfeld, “Theoretical considerations on the motion of salt and fresh water”, in *Proceedings Minnesota International Hydraulic Convention*, IAHR, 1953, pp. 321–333.
- [37] L. Armi, “The hydraulics of two flowing layers with different densities”, *J. Fluid Mech.* **163** (1986), pp. 27–58.
- [38] D. Z. Zhu and G. A. Lawrence, “Hydraulics of exchange flows”, *J. Hydraul. Eng.* **126** (2000), no. 12, pp. 921–928.
- [39] L. Gu and G. A. Lawrence, “Analytical solution for maximal frictional two-layer exchange flow”, *J. Fluid Mech.* **543** (2005), pp. 1–17.
- [40] L. Zhu, A. Atoufi, A. Lefauve, J. R. Taylor, G. A. Lawrence, S. B. Dalziel, R. R. Kerswell and P. F. Linden, “Stratified inclined duct: direct numerical simulations”, *J. Fluid Mech.* **969** (2023), article no. A20.



- [41] A. Atoufi, L. Zhu, A. Lefauve, et al., “Stratified inclined duct: two-layers hydraulics and instabilities”, *J. Fluid Mech.* **977** (2023), article no. A25.
- [42] J. L. Partridge, A. Lefauve and S. B. Dalziel, “A versatile scanning method for volumetric measurements of velocity and density fields”, *Meas. Sci. Tech.* **30** (2019), article no. 055203.
- [43] A. Lefauve and P. F. Linden, *Research data supporting “Experimental properties of continuously-forced, shear-driven, stratified turbulence”*, dataset, Apollo - University of Cambridge Repository (February 7, 2022). <https://doi.org/10.17863/CAM.75370>, 2022.
- [44] S. B. Dalziel, M. Carr, J. K. Sveen and P. A. Davies, “Simultaneous synthetic schlieren and PIV measurements for internal solitary waves”, *Meas. Sci. Tech.* **18** (2007), no. 3, pp. 533–547.
- [45] A. Lefauve, J. L. Partridge and P. F. Linden, *Research data supporting “Regime transitions and energetics of sustained stratified shear flows”*, dataset, Apollo - University of Cambridge Repository (July 22, 2019). <https://doi.org/10.17863/CAM.41410>, 2019.
- [46] K. B. Winters, P. N. Lombard, J. J. Riley and E. A. D’Asaro, “Available potential energy and mixing in density-stratified fluids”, *J. Fluid Mech.* **289** (1995), pp. 115–128.
- [47] A. Lefauve, J. L. Partridge and P. F. Linden, “Regime transitions and energetics of sustained stratified shear flows”, *J. Fluid Mech.* **875** (2019), pp. 657–698.
- [48] A. Lefauve and P. F. Linden, “Experimental properties of continuously forced, shear-driven, stratified turbulence. Part 2. Energetics, anisotropy, parameterisation”, *J. Fluid Mech.* **937** (2022), article no. A35.
- [49] M. C. Cross and P. C. Hohenberg, “Pattern formation outside of equilibrium”, *Rev. Mod. Phys.* **65** (1993), no. 3, pp. 851–1112.
- [50] D. Barkley, “Theoretical perspective on the route to turbulence in a pipe”, *J. Fluid Mech.* **803** (2016), article no. P1.
- [51] W. D. Smyth and J. R. Carpenter, *Instability in Geophysical Flows*, Cambridge University Press, 2019.
- [52] J. R. Carpenter, E. W. Tedford, E. Heifetz and G. A. Lawrence, “Instability in stratified shear flow: Review of a physical interpretation based on interacting waves”, *Appl. Mech. Rev.* **64** (2011), no. 6, article no. 060801.
- [53] J. Cudby and A. Lefauve, “Weakly nonlinear Holmboe waves”, *Phys. Rev. Fluids* **6** (2021), no. 2, article no. 024803.
- [54] Y.-M. Ducimetière, F. Gallaire, A. Lefauve and C. P. Caulfield, “The effects of spanwise confinement on stratified shear instabilities”, *Phys. Rev. Fluids* **6** (2021), article no. 103901.
- [55] H. Salehipour, C. P. Caulfield and W. R. Peltier, “Turbulent mixing due to the Holmboe wave instability at high Reynolds number”, *J. Fluid Mech.* **803** (2016), pp. 591–621.
- [56] H. Van Haren, “Stratified turbulence and small-scale internal waves above deep-ocean topography”, *Phys. Fluids* **25** (2013), no. 10, article no. 106604.
- [57] A. Kaminski, E. A. D’Asaro, A. Y. Shcherbina and R. R. Harcourt, “High-Resolution Observations of the North Pacific Transition Layer from a Lagrangian Float”, *J. Phys. Oceanogr.* **51** (2021), no. 10, pp. 3163–3181.
- [58] P. Held, K. Bartholomä-Schrottke and A. Bartholomä, “Indications for the transition of Kelvin-Helmholtz instabilities into propagating internal waves in a high turbid estuary and their effect on the stratification stability”, *Geo-Mar. Lett.* **39** (2019), no. 2, pp. 149–159.
- [59] A. Mashayek and W. R. Peltier, “The ‘zoo’ of secondary instabilities precursory to stratified shear flow transition. Part 1: Shear aligned convection, pairing, and braided instabilities”, *J. Fluid Mech.* **708** (2012), pp. 5–44.
- [60] L. Zhu, A. Atoufi, A. Lefauve, R. R. Kerswell and P. F. Linden, “Long-wave instabilities of sloping stratified exchange flows”, *J. Fluid Mech.* **983** (2024), article no. A12.
- [61] G. Kawahara, M. Uhlmann and L. van Veen, “The Significance of Simple Invariant Solutions in Turbulent Flows”, *Ann. Rev. Fluid Mech.* **44** (2012), no. 1, pp. 203–225.
- [62] M. D. Graham and D. Floryan, “Exact Coherent States and the Nonlinear Dynamics of Wall-Bounded Turbulent Flows”, *Ann. Rev. Fluid Mech.* **53** (2021), pp. 227–253.
- [63] P. Cvitanović, “Recurrent flows: the clockwork behind turbulence”, *J. Fluid Mech.* **726** (2013), pp. 1–4.
- [64] D. Lucas, C. P. Caulfield and R. R. Kerswell, “Layer formation in horizontally forced stratified turbulence: connecting exact coherent structures to linear instabilities”, *J. Fluid Mech.* **832** (2017), pp. 409–437.
- [65] X. Jiang, A. Lefauve, S. B. Dalziel and P. F. Linden, “The evolution of coherent vortical structures in increasingly turbulent stratified shear layers”, *J. Fluid Mech.* **937** (2022), A30.
- [66] P. J. Schmid, “Data-driven and operator-based tools for the analysis of turbulent flows”, in *Advanced Approaches in Turbulence*, Elsevier, 2021, pp. 243–305.
- [67] C. P. Caulfield, W. R. Peltier, S. Yoshida and M. Ohtani, “An experimental investigation of the instability of a shear flow with multilayered density stratification”, *Phys. Fluids* **7** (1995), no. 12, pp. 3028–3041.
- [68] T. S. Eaves and N. J. Balmforth, “Noisy homoclinic pulse dynamics”, *Chaos* **26** (2016), no. 4, article no. 043104.
- [69] W. R. Geyer and P. MacCready, “The Estuarine Circulation”, *Ann. Rev. Fluid Mech.* **46** (2014), no. 1, pp. 175–197.
- [70] F. Chegini et al., “Processes of Stratification and Destratification During An Extreme River Discharge Event in the German Bight ROFI”, *J. Geophys. Res. Oceans* **125** (2020), no. 8, article no. e2019JC015987.
- [71] W. D. Smyth, J. N. Moum, L. Li and S. A. Thorpe, “Diurnal shear instability, the descent of the surface shear layer, and the deep cycle of equatorial turbulence”, *J. Phys. Oceanogr.* **43** (2013), no. 11, pp. 2432–2455.

- [72] W. D. Smyth, H. T. Pham, J. N. Moum and S. Sarkar, "Pulsating turbulence in a marginally unstable stratified shear flow", *J. Fluid Mech.* **822** (2017), pp. 327–341.
- [73] L. Mahrt, "Stably Stratified Atmospheric Boundary Layers", *Ann. Rev. Fluid Mech.* **46** (2014), no. 1, pp. 23–45.
- [74] H. Salehipour, W. R. Peltier and C. P. Caulfield, "Self-organized criticality of turbulence in strongly stratified mixing layers", *J. Fluid Mech.* **856** (2018), pp. 228–256.
- [75] P. Bak, C. Tang and K. Wiesenfeld, "Self-organized criticality", *Phys. Rev. A* **38** (1988), no. 1, pp. 364–374.
- [76] W. D. Smyth, "Marginal Instability and the Efficiency of Ocean Mixing", *J. Phys. Oceanogr.* **50** (2020), no. 8, pp. 2141–2150.
- [77] A. Mashayek, L. E. Baker, B. B. Cael and C. P. Caulfield, "A Marginal Stability Paradigm for Shear-Induced Diapycnal Turbulent Mixing in the Ocean", *Geophys. Res. Lett.* **49** (2022), no. 2, article no. e2021GL095715.
- [78] D. Bouffard and L. Boegman, "A diapycnal diffusivity model for stratified environmental flows", *Dyn. Atmos. Oceans* **61-62** (2013), pp. 14–34.
- [79] L. Cimoli, C. P. Caulfield, H. K. Johnson, D. P. Marshall, A. Mashayek, A. C. Naveira Garabato and C. Vic, "Sensitivity of Deep Ocean Mixing to Local Internal Tide Breaking and Mixing Efficiency", *Geophys. Res. Lett.* **14** (2019), pp. 14622–14633.
- [80] R. C. Holleman, W. R. Geyer and D. K. Ralston, "Stratified Turbulence and Mixing Efficiency in a Salt Wedge Estuary", *J. Phys. Oceanogr.* **46** (2016), no. 6, pp. 1769–1783.
- [81] M. Meredith and A. C. Naveira Garabato, *Ocean Mixing: Drivers, Mechanisms and Impacts*, Elsevier, 2021.
- [82] A. Mashayek, H. Salehipour, D. Bouffard, C. P. Caulfield, R. Ferrari, M. Nikurashin, W. R. Peltier and W. D. Smyth, "Efficiency of turbulent mixing in the abyssal ocean circulation", *Geophys. Res. Lett.* **44** (2017), no. 12, pp. 6296–6306.
- [83] N. Petropoulos, M. M. P. Couchman, A. Mashayek, S. M. De Bruyn Kops and C. P. Caulfield, "Prandtl number effects on extreme mixing events in forced stratified turbulence", *J. Fluid Mech.* **983** (2024), article no. R1.
- [84] G. Brethouwer, P. Billant, E. Lindborg and J.-M. Chomaz, "Scaling analysis and simulation of strongly stratified turbulent flows", *J. Fluid Mech.* **585** (2007), pp. 343–368.
- [85] S. M. de Bruyn Kops, "Classical scaling and intermittency in strongly stratified Boussinesq turbulence", *J. Fluid Mech.* **775** (2015), pp. 436–463.
- [86] G. K. Batchelor, "Small-scale variation of convected quantities like temperature in turbulent fluid Part 1. General discussion and the case of small conductivity", *J. Fluid Mech.* **5** (1959), no. 01, pp. 113–133.
- [87] W. R. Geyer, M. E. Scully and D. K. Ralston, "Quantifying vertical mixing in estuaries", *Environ. Fluid Mech.* **8** (2008), no. 5-6, pp. 495–509.
- [88] P. R. Jackson and C. R. Rehmann, "Experiments on Differential Scalar Mixing in Turbulence in a Sheared, Stratified Flow", *J. Phys. Oceanogr.* **44** (2014), no. 10, pp. 2661–2680.
- [89] G. D. Portwood, S. M. de Bruyn Kops and C. P. Caulfield, "Asymptotic dynamics of high dynamic range stratified turbulence", *Phys. Rev. Lett.* **122** (2019), article no. 194504.
- [90] L. Zhu, X. Jiang, A. Lefauve, R. R. Kerswell and P. F. Linden, "New insights into experimental stratified flows obtained through physics-informed neural networks", *J. Fluid Mech.* **981** (2024), article no. R1.